

A Stochastic Geometry Framework for Performance Analysis of RIS-assisted OFDM Cellular Networks

Guodong Sun, François Baccelli, Ke Feng, Luis Uzeda Garcia, Stefano Paris

Abstract

The reconfigurable intelligent surface (RIS) technology allows one to engineer spatial diversity in complex cellular networks. This paper provides a framework for the system-level performance assessment of RIS-assisted networks and in particular downlink coverage probability and ergodic rate. To account for the inherent randomness in the spatial deployments of base stations (BSs) and RISs, we model the placements of the RISs as point processes (PPs) conditioned on the associated BSs, which are modeled by a Poisson point process (PPP). These RIS PPs can be adapted based on the deployment strategy. We focus on modeling the RISs as a Matérn cluster process (MCP), where each RIS cluster is a finite PPP with support of a disc centered on the association BS. We assume that the system uses the orthogonal frequency division multiplexing (OFDM) technique to exploit the multipath diversity provided by RISs. The coverage probability and the ergodic rate can be evaluated when RISs operate as batched powerless beamformers. The resulting analytical expressions provide a general methodology to evaluate the impact of key RIS-related parameters, such as the batch size and the density of RISs, on system-level performance. To demonstrate the framework's broad applicability, we also analyze a RIS placement variant where RISs are deployed around coverage holes. Numerical evaluations of the analytical expressions and Monte-Carlo simulations jointly validate the proposed analytical approach and provide valuable insights into the design of future RIS-assisted cellular networks.

Index Terms

Reconfigurable Intelligent Surfaces, Stochastic Geometry, Point Process, Matérn Cluster Process, Orthogonal Frequency Division Multiplexing, Diversity Combining.

I. INTRODUCTION

The upcoming sixth-generation (6G) networks aim for higher energy efficiency without adding complexity or energy consumption [1]–[6]. To achieve this, the RIS technology, leveraging a large number of passive elements,

G. Sun, F. Baccelli, K. Feng are with Institut national de recherche en sciences et technologies du numérique (INRIA), 2 Rue Simone IFF, 75012 PARIS, and with Department d'information, Ecole Normale Supérieure, 45 Rue d'Ulm, 75005, PARIS.(email: guodong.sun | francois.baccelli@ens.fr, ke.feng@inria.fr.)

G. Sun, L. Garcia, S. Paris are with Nokia Networks France, 12 Rue Jean Bart 91300 MASSY. (email: guodong.sun | luis.uzeda_garcia | stefano.paris@nokia.com.)

This paper was submitted to the IEEE Transactions on Wireless Communications.

represents a promising candidate for transforming the radio propagation environment to a controllable one with minimal power consumption [7]–[9]. Similar to the relay technology, the RIS technology can enhance spatial diversity by providing alternative propagation paths for the signal, enabling control over the radio propagation environment [9], [10]. In [11], [12], comparative studies between RIS and relay reveal key advantages of RIS in terms of energy efficiency, spectrum efficiency, and implementation complexity.

Compared to half-duplex relays, a RIS extends the classical channel between a BS and user equipment (UE) with the creation of additional paths [11]. For the RIS-assisted channel, which is time-dispersive since the direct and the RIS-reflected signals may not arrive at the same time due to the distance difference of the radio wave propagation, the intersymbol interference (ISI) becomes a significant issue [13], [14]. The OFDM modulation technique, introduced to cellular networks since the fourth generation (4G) long-term evolution (LTE) [15], can efficiently render the multipath channel ISI-free [16]. To characterize the channel model for RIS-assisted communication links, the authors in [17] show that only the direct link (i.e., the link between the BS and the UE) and the controllable reflected link (i.e., the link passing through the RIS) should be explicitly modeled, whereas the scattered signal from the environment can be neglected in the link-level performance evaluation and optimization. The authors in [18] use optical physics to derive a far-field pathloss model, where the reflective elements of the RIS jointly beamform the signal in a desired direction when the elements individually act as diffuse scatterers. In addition, channel acquisition in the presence of RIS requires the estimation of the multiple components of the reflected link, for which iterative protocols and algorithms as proposed in [19] can be employed.

RIS operate in multiple ways, and several techniques have been explored to enhance the link-level performance of the channel composed of direct and reflected paths. For example, the authors in [20] and [21] investigate the problem of optimizing the beamforming gain of the combined direct and reflected channel assuming an ideal phase-shift model for RIS elements and propose iterative optimization methods to compute the optimal phase-shift configuration of a RIS. The optimal configuration of RIS-assisted networks is studied in [22], where the authors formulate and evaluate the optimization problem of selecting the orientation and location of the RIS to extend the coverage area of a single designated user. A finite resolution phase shift model is evaluated in [23], where the reflection is designed to have the maximum phase alignment at the designated receiver. On the other hand, more complex techniques exploit RISs to cancel interference at a defined user or to dynamically modulate the phases of RIS elements to carry information. In [24], the authors deploy a RIS to assist an indoor multi-user system, improving the overall system performance by canceling the interference and enhancing the users' signal quality. In [25], an iterative optimization is proposed to maximize the minimum signal-to-noise-and-interference ratio (SINR) among multiple users in the MISO communication system. The authors in [21] observe that RISs should be deployed close to either the transmitter or the receiver to maximize the beamforming gain.

The challenge of characterizing the system performance leveraging the concept of relaying signals via separated propagation paths based on stochastic geometry can be traced back to the research on relays, e.g., [26], [27]. This task remains challenging in the age of RIS. Preliminary works on the system-level performance analysis of RIS-assisted wireless networks show that adding RISs in the network can increase the coverage of wireless networks and the area spectral efficiency (ASE) [28], [29]. For instance, the authors in [29] study the impact of mounting

RISs on obstacles like buildings, street lamps, and traffic lights and derive a combinatorial solution to compute the overall probability of line-of-sight communication. The authors in [30] evaluate the probability of successful signal reflection according to the spatial distribution and orientation of RISs using a Boolean line segment model. The authors in [31] investigate the RIS placement problem to have high coverage probability in a street using a simplified one-dimensional (1D) stochastic geometry model. The work concludes that RISs should be placed on the street intersections to increase coverage probability. While these results provide some useful insights for the system-level deployment of RISs like the optimal density of BSs and RISs to maximize coverage probability, the impact of several key properties of RISs as well as the correlation between BSs and RISs positions have not been investigated yet.

Furthermore, general analytical results are still missing. For example, the authors in [32] model both BSs and RISs as homogeneous PPPs and associate the typical UE to the nearest BS and RIS. With similar setups, the authors in [33] investigate RIS-assisted multi-cell non-orthogonal multiple access (NOMA) networks. To consider the spatial correlation between RISs and BSs, the authors in [34] use the Gauss-Poisson process to model the BSs and RISs. These works [32]–[34] approximate the composite signal by a Gamma distribution using the moment matching method conditioned on a specific system layout and then integrate it over all possible layouts. Namely, the BS-RIS pair is treated as a whole by abstracting their spatial distribution. In [35], the authors model the composition of a direct link and a reflected as the sum of two exponential distributions, leveraging the property of Erlang distribution. Although this work provides accurate distribution of the composite signal, they however focus on the case where both the direct and reflected links experience Rayleigh fading and the spatial randomness still requires iterative integration. For the case where UE is served by more than a single RIS, the iteration of integration steps becomes intractable. In [12], the authors point out that performance analysis for the networks where a multitude of RISs serve UEs is an open challenge.

A. *Motivation and Contribution*

The present paper uses stochastic geometry, which is an analytical framework to investigate and design systems, as demonstrated in [36]–[38]. A key advantage of this approach lies in its ability to express performance metrics in terms of the Laplace transform of the aggregated interference-noise, as shown in [39]. When RISs play a constructive role in system performance, stochastic geometry calls for a framework that should be capable of analyzing system performance metrics by considering the combined effects of signals (direct and reflected), interference, and noise, expressed through their Laplace transforms. In the literature, the reflected signal is merged into the direct link. The composite signal can only be accurately characterized when both links are modeled as Rayleigh distributed, resulting in an Erlang distributed signal [35]. Otherwise, the composite signal is approximated by a Gamma distribution using the moments matching method [32]–[34]. The signal merging mechanism fails when increasing the number of RISs in an area since the possible spatial layout grows exponentially in function of the number of RIS and the computation becomes intractable. Motivated by the above discussion,

- we propose an analytical framework that can analyze the random deployment of several RISs in an area to assist the existing cellular network. This framework is flexible. For instance, the number of RISs can be

either random (modeling using a PPP) or fixed (modeling using a BPP). The RIS placement area, defined by the support of the RIS PP, can be adapted to different deployment strategies. We focus on the study of the scenario where RISs are deployed around the BSs and extend to a variant accounting for alleviating coverage holes. The main contribution is hence a general method to evaluate these RIS-assisted networks by analytically characterizing the composite signal and deriving the spectral efficiency in this context. This allows one to assess the role RISs play at a system level.

- The main novelty is the modeling of the *reflected signals from several RISs as a shot noise field* that comes in addition to the classical stochastic geometry setting where only the interference is considered as a shot noise field. The *signal shot noise field* models the reflected links from several randomly located RISs associated with the serving BS to the UE. The impact of the signal-interference-noise competition can be modeled as the difference between two non-negative random variables, one for the aggregated interference and noise and the other for the aggregated reflected signals, so that the resulting random variable is defined over the whole real line. To derive the coverage probability, the difficulty lies in separating the negative and positive parts of this random variable from the knowledge of its Laplace transform. We use the general analytical approach based on the contour integral method to solve this separation problem and to derive the coverage probability and the spectral efficiency. Key performance metrics can then be easily expressed from this analysis.
- This methodology allows one to quantitatively answer system-level questions when RISs are randomly deployed. For instance, while RISs can benefit the intended signals, will it also significantly increase system-level interference? If yes, how much? Under which condition can this be negligible? How do the geometric parameters impact the system's performance? Deploying RIS strategically will enhance coverage in certain areas, what are the best deployment strategies?

B. Organization

The paper is organized as follows: we define the major components for modeling RIS-assisted networks in Section II, including the random placements of both BSs and RISs and the fading of individual links. In Section III, we discuss signal processing and system performance assessments for a special deployment strategy where the RISs are modeled as an MCP. We then extend this special but fundamental case to consider various RIS placement strategies in Section IV, incorporating various deployment concerns. We present extensive simulations and numerical results in Section V and the paper is concluded in Section VI.

Table I summarizes the notation used in this work. Throughout this work, we use Greek letters in general to denote the random variables associated with channel fading.

II. MAJOR COMPONENTS OF FRAMEWORK

As depicted in the system figure (Fig. 1), randomly located BSs form a cellular network in the two-dimensional (2D) Euclidean space, modeled by a PPP. The coverage region of a BS is the Voronoi cell of this BS. Each cell is equipped with a set of RISs, which is modeled as a conditionally independent PP. In this section, to study the performance of downlink communications assisted by RISs, we characterize the links for the direct signal and

TABLE I: Lists of Notations

Notation	Meaning
$\lambda_{\{\cdot\}}$	Density of UEs, BSs, RISs.
$\mathbf{x}_i \in \Phi_{\text{BS}}$	i th BS in the BS set.
$i \in \mathcal{I}$	Index set of the BSs and their associated RISs.
$\mathbf{y}_{i,j} \in \phi_i$	j th RIS in i th cluster. (o for the typical one).
$j \in \mathcal{J}_i$	Index set of the RISs for ϕ_i .
o	Subscripts to specify the relationship to the typical UE.
$\mathbb{D}_{\mathbf{x}_i}$	Ring cluster centered at \mathbf{x}_i .
$R_{\text{in}}, R_{\text{out}}$	Inner and outer radius of the RIS cluster.
M, m	Number and index of elements in a RIS.
M_o	Number of elements allocated to the typical UE.
θ, Θ	RIS configuration scalar and matrix.
ϑ	Beamwidth of reflected beam from a RIS.
P_0	Transmit power per BS for a UE.
Q_S, Q_I, σ_w^2	Power of signal, interference, and noise.
Q_c	Power of interference from a RIS cluster.
$Z[n], \mathcal{Z}[k]$	Channel's function in time and frequency domain.
$g(d), \alpha, \beta$	Pathloss of a link, with exponent and antenna gain.
$G(\mathbf{x}, \mathbf{y})$	Pathloss of a reflected link (vector).
$\mathcal{G}(x, y, \psi)$	Pathloss of a reflected link (scalar).
B	Carrier's bandwidth.
T_s	Antenna sampling time.
$\delta[n]$	Kronecker delta function.
h	Channel gain for individual links.
\hat{h}	Channel gain computed for codewords.
$\rho \in \mathbb{C}$	Random variable for small fading.
$\zeta \in \mathbb{C}$	Random variable as the product of two i.i.d. ρ .
$\eta \in \mathbb{C}$	Random variable as the sum of ζ .
$\mathcal{N}(\mu, \sigma^2)$	Gaussian random variable with mean and variance.
χ^2	Chi-square distributed random variable.
$\mathbb{E}[\cdot], \mathbb{V}[\cdot]$	Operators to obtain expectation and variance.
γ	Fading power of the specific links.
D, R	Superscripts to denote the direct or the reflected link.
i	Imaginary unit.
\mathcal{L}_f	Unilateral Laplace transform of function f .
\mathcal{B}_f	Bilateral Laplace transform of function f .
s, \bar{s}	Transmitted and received signal.
$\mathbf{s}, \bar{\mathbf{s}}$	Signal representation in frequency domain.
N_s	Length of the symbol block.
N_c	Length of the discrete channel impulse response.
P_c	Coverage probability.
r	Distance to the associated BS from the typical UE.
T	SIR threshold above which transmission is successful.
τ	Ergodic rate [nat/Hz/s].
C_D, C_R	Blockage penalty for the direct and reflect links.
$[-\varpi, \varpi]$	Angle spans a wedge-shaped area.

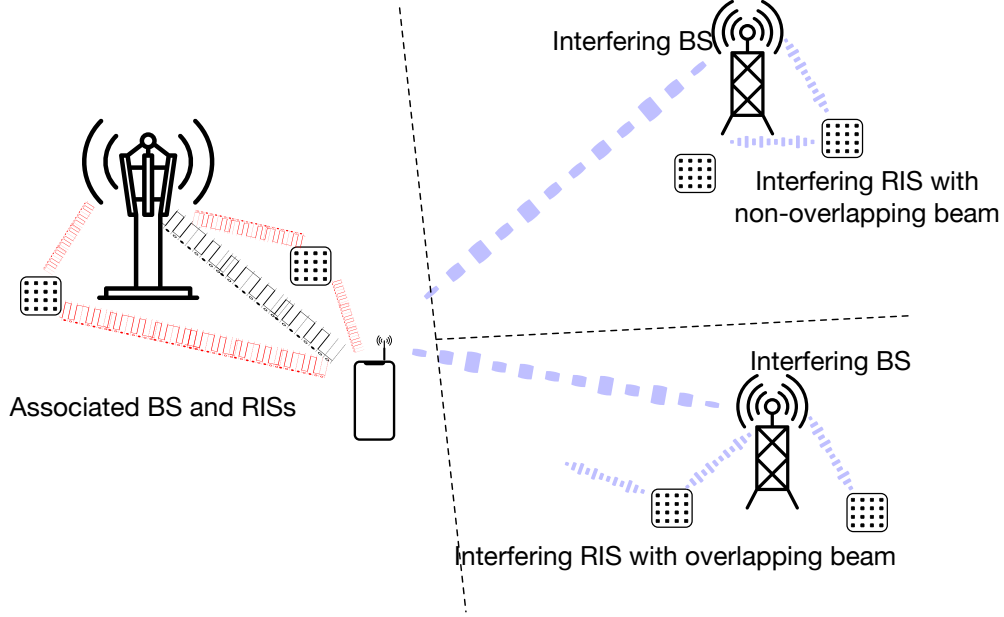


Fig. 1: An illustration of a cellular network, where RISs intelligently reflect signals from the associated BSs for their associated UEs, while the interference from the BSs and RISs in neighboring cells can also reach the UEs.

reflected signals, preparing for system performance evaluation in the next section. We also characterize the links for the direct signal and reflected interference since BSs and RISs create interference for UEs in other cells.

A. Spatial model and RIS model

The location of BSs is modeled as a homogeneous PPP $\Phi_{\text{BS}} \triangleq \mathbf{x}_i, i \in \mathcal{I}$, with density λ_{BS} , where \mathcal{I} is the index set of the BSs. Here, BSs transmit signals in all directions to reach randomly located UEs and RISs. We assume that the UEs are served by their closest BS, and this association policy divides the cellular network into Voronoi cells with respect to (w.r.t.) Φ_{BS} . Since RISs are network infrastructure entities, we assume that they are associated with individual cells and managed by the corresponding BS. We model the RISs in the Voronoi cell associated with the i^{th} BS by a conditionally independent PP $\mathbf{y}_{i,j} \in \phi_i, j \in \mathcal{J}_i$, where $\mathbf{y}_{i,j}$ specifies the location of the j^{th} RIS and \mathcal{J}_i is the corresponding index set. In simpler terms, we consider the placement of RISs independently for each cell, only depending on the location of the BS \mathbf{x}_i . Then, the overall RISs are modeled as the aggregation of the conditionally independent PPs, $\Phi_{\text{RIS}} \triangleq \cup \phi_i, i \in \mathcal{I}$. The placement of RISs, i.e., the distribution of PP and its support, is determined by specific deployment strategies, which will be defined in the next two sections.

In this work, we focus on a typical UE that represents UEs satisfying the far-field condition with respect to the RIS. The physical size of RIS plays a role in choosing an appropriate channel model between near-field and far-field regimes. When the RIS size is comparable to the distance between the RIS and the UE/BS, the shape of the wavefront experienced by the RIS or reflected from the RIS cannot be considered planar. For system-level analysis, we focus on the far-field model to simplify calculations, which is applicable when the RIS size is significantly smaller than the distance between the RIS and the BS/UE. To ensure the far-field condition, our stochastic geometry model

incorporates distance guards between the RIS and BS/UE, which restrict possible layouts of the RIS-assisted cellular network. We denote the BS to which the typical UE is associated with by \mathbf{x}_o and the corresponding PP for RISs by ϕ_o (to facilitate notation, we will also index the signals and channels associated with the typical UE by o). We assume that RISs are divided into small batches for a system-level service and multiple RISs can serve the typical UE simultaneously. In addition, each BS uses orthogonal multiple access within each Voronoi cell, so there is no intra-cell interference.

We now discuss the model for RIS beamforming. Several types of RISs are specified in the standard [40], in which general operation principles such as reflecting, refracting, and scattering are discussed. According to the deployment scenarios, RIS can either be a reflecting surface that can serve the UE when the BS is located on the same side of the surface, or be a refracting surface when it is located on the other side. Since we model RISs by PPs and neglect the dimension, i.e., the width and the length of RISs, thus the side or type information is neglected in this modeling. Without loss of generality, we assume that the RISs are capable of serving the associated UEs properly and we thus use the term ‘‘isotropic reflection/refraction’’ to cover both cases, in which each RIS can virtually reflect or refract the signal in any direction with a specified RIS-UE association. Refined models taking into account the nature of the RISs (reflective or refractive) can be analyzed by the same method by changing the density of RISs.

We assume that a RIS has M ideal reflecting elements, where each RIS element allows both perfect radio reflection or refraction without energy loss and acts as an isotropic lossless phase shifter that can scatter the absorbed energy with a controllable phase shift [21], [41]. In particular, the configuration profile of the RIS located at $\mathbf{y}_{i,j}$ is denoted by a diagonal matrix of unitary phase-shifts

$$\Theta_{\mathbf{y}_{i,j}} = \text{diag}\{e^{i\theta_{\mathbf{y}_{i,j}}^{(1)}}, \dots, e^{i\theta_{\mathbf{y}_{i,j}}^{(m)}}, \dots, e^{i\theta_{\mathbf{y}_{i,j}}^{(M)}}\}, \quad (1)$$

where $\theta_{\mathbf{y}_{i,j}}^{(m)} \in [0, 2\pi)$ specifies the phase shift of the reflected signal against the incident signal for the m^{th} element in the j^{th} RIS in the i^{th} cell.

Within a Voronoi cell, the deployment of RISs aims to create favorable signal propagation conditions, like line-of-sight (LoS) channels, to provide the reflected links between the BS and the UEs of that cell. This strategic positioning is however not intended for the reflections of the signals originating from other cells, whether from their BS or RISs. In fact, for any given RIS, incoming signals from other cells will be negligible compared to the signal from its serving BS, since the high path loss and lower likelihood of LoS propagation between cells make such reflection significantly weak. Consequently, we can assume that each RIS primarily reflects signals from its associated BS.

B. Signal and channel model

In this subsection, we discuss the signal propagation model. We will discuss the signal processing performed by the UE in the next section. To account for the channels for signal propagation from the associated BS to the typical UE, we focus on the strongest channel tap for each engineered path [42]. In other words, each link between

a pair of nodes among BS, RIS, and UE. is modeled as a single channel tap. We denote the sampling rate¹ of the antennas by $\frac{1}{T_s}$, which is used to resolve the delays of different paths. Since the multiple RISs serving the typical UE are randomly distributed, the intended signal transmitted from the BS arrives at the typical UE with different resolvable delays, and thus the RIS-assisted channel can be assumed to be in the class of time-dispersive wideband communication [14], [43].

We assume that the channels are approximately constant during the transmission block and thus the channel gains are time-independent. Specifically, we denote the channel gains as $h_{D_i} \in \mathbb{C}$, $\mathbf{h}_{R_{1,i,j}} \in \mathbb{C}^M$, and $\mathbf{h}_{R_{2,i,j}} \in \mathbb{C}^M$ for the direct link from the i^{th} BS to the typical UE, with superscript D_i , for the reflected link from the i^{th} BS to j^{th} RIS, with the superscript $R_{1,i,j}$, and for the link from that RIS to the typical UE, $R_{2,i,j}$, respectively. Here, the dimension M of $\mathbf{h}_{R_{1,i,j}}$ and $\mathbf{h}_{R_{2,i,j}}$ refers to the number of RIS elements in each RIS. The discrete-time channel impulse response from the i^{th} BS is modeled by a tapped-delay line filter, in which every delayed tap represents the strongest channel tap of either the direct path or one of the reflected paths, expressed by

$$Z_i[n] = h_{D_i} \delta[n - n_{D_i}] + \sum_{\mathbf{y}_{i,j} \in \phi_i} \mathbf{h}_{R_{2,i,j}}^H \Theta_{\mathbf{y}_{i,j}} \mathbf{h}_{R_{1,i,j}} \delta[n - n_{R,i,j}], \quad (2)$$

for $n \in [N_c]$, $i \in \mathcal{I}$, where $n_{D_i} = \lfloor \frac{\|\mathbf{x}_i\|}{cT_s} \rfloor$ denotes the discrete time delay of the direct channel from the i^{th} BS and $n_{R,i,j} = \lfloor \frac{\|\mathbf{x}_i - \mathbf{y}_{i,j}\| + \|\mathbf{y}_{i,j}\|}{cT_s} \rfloor$ denotes the delay of the reflected channel via the j^{th} RIS in the i^{th} cell. Here, $\delta[n - n_{D_i}]$ denotes the time-delay Kronecker delta function, c is the speed of light, $\lfloor \cdot \rfloor$ denotes the floor operator, $\{\cdot\}^H$ is the Hermitian conjugate, and the abbreviation $[N]$ stands for $\{0, 1, \dots, N - 1\}$. Furthermore, we assume that different nodes create resolvable paths with different delays, i.e., no two of the delays $n_{D_i}, n_{R,i,j}$ coincide. For our purpose, there is no need to specify the direct and the reflected paths since the OFDM modulation and demodulation are performed blockwise, which will be discussed in the next section². Note that some taps of the sequence $Z_i[n]$ are zeros when there is no significant path at these sampling delays and this fact is taken into account in the remaining discussion. The length of the tapped delay line filter is denoted as N_c , spanning the delay spread of the time-dispersive channel.

To describe the characteristics of individual links, we assume a simplified fading channel model that comprises the signal power attenuation $g(d)$ described in what follows and small-scale fadings ρ discussed in the next subsection. Here, d is the Euclidean distance between the two nodes. Consequently, the entry in the channel gain vector h_{D_i} is given by

$$h_{D_i} = \rho_{D_i} \cdot \sqrt{g(\|\mathbf{x}_i\|)} \in \mathbb{C}, i \in \mathcal{I}. \quad (3)$$

Similarly, the entries of the channel gain matrices for the reflected link $\mathbf{h}_{R_{1,i,j}}$ and $\mathbf{h}_{R_{2,i,j}}$ are given by

$$\mathbf{h}_{R_{1,i,j}}^{(m)} = \rho_{R_{1,i,j}}^{(m)} \cdot \sqrt{g(\|\mathbf{y}_{i,j}\|)} \in \mathbb{C}, i \in \mathcal{I}, j \in \mathcal{J}, m \in [M], \quad (4)$$

¹This is the rate with which the antenna is able to resolve the time delays of the signal traveling via the direct path and the different reflected paths provided by RISs. For example, in the 5G standard, an antenna should support a sampling rate of up to 0.509ns, which allows the antenna to resolve the signal passing through the different paths with a distance difference of 0.15 meters. This distance is smaller than the distance between usual physical nodes, and hence the antenna can resolve different signal paths.

²Without loss of generality, the train of the taps is not ordered since the precedence of the paths is not clear.

and

$$\mathbf{h}_{R_{2,i,j}}^{(m)} = \rho_{R_{2,i,j}}^{(m)} \cdot \sqrt{g(\|\mathbf{x}_i - \mathbf{y}_{i,j}\|)} \in \mathbb{C}, i \in \mathcal{I}, j \in \mathcal{J}, m \in [M], \quad (5)$$

where the additional superscript (m) denotes the index of the m^{th} element in the RIS as in Eq. (1).

The signal power attenuation between two nodes is modeled by a distance-dependent model with path-loss exponent $\alpha > 2$, given by

$$g(d) = \beta(d+1)^{-\alpha}, \quad (6)$$

where $\beta = \frac{c}{4\pi f_c}$ is the average power gain received by an isotropic receiving antenna at a reference distance of 1m based on the free-space path-loss model, f_c is the carrier frequency, and c denotes the speed of light. We select this path loss model to avoid the singularity issue of the fraction of $d^{-\alpha}$ when $d \rightarrow 0$. The reflected links experience multiplicative pathloss [18], denoted by $G(\mathbf{x}, \mathbf{y}) = g(\|\mathbf{y}\|)g(\|\mathbf{x} - \mathbf{y}\|)$, $\mathbf{x}, \mathbf{y} \in \mathbb{R}^2$, where $\mathbf{x} \in \Phi_{\text{BS}}, \mathbf{y} \in \Phi_{\text{RIS}}$ are the coordinates of the nodes.

The above channel model features two distinct multipath phenomena in RIS-assisted cellular networks: the signal propagation over the engineered paths provided by RISs and over the paths due to random environmental reflections and scattering. On the one hand, RISs provide engineered propagation paths by performing beamforming. This type of path is critical for the properties of RIS-assisted networks, as the signal strength over these paths is expected to be stronger than random environmental reflections and scattering. Additionally, since RIS deployments typically involve entities separated by several meters, the propagation delays introduced by these engineered paths could be resolved by the antenna. On the other hand, each resolvable path between two nodes experiences random reflections and scattering near the receiving nodes. Note that small-scale fading is mainly due to the cluster of scatterers concentrated around the receiving node. This type of multipath has no significant delay and can be superposed to cause fluctuation, known as small-scale fading. This phenomenon primarily affects individual links³. As previously assumed, other environmental reflections experiencing significant propagation delay also undergo high power attenuation and are therefore neglected.

C. The fading of the direct and reflected signals

To analyze the role of RISs on the performance of the UEs that experience unfavorable propagation, we consider two key characteristics of signal propagation in channel modeling: line-of-sight (LoS) conditions and fading. We model the direct links between BSs and UEs as experiencing non-line-of-sight (NLoS) propagation and the fading $\rho_D \in \mathbb{C}$ is modeled as Rayleigh distributed. Given that RISs are strategically deployed to create LoS channels for UEs within their designated cell, we model the channels between the BS and its associated RISs and the channels between these RISs and the associated UE as LoS links, where the corresponding fading denoted by $\rho_{R_{1,o,j}} \in \mathbb{C}$, $\rho_{R_{1,i,j}} \in \mathbb{C}$, and $\rho_{R_{2,o,j}} \in \mathbb{C}$ are modeled as Rician distribution. On the other hand, the links between the RISs and

³We assume that the scattered signals from far-away objects with large time delays are neglected due to the severe propagation loss. The fading of all the reflected channels via the reflecting elements at the same RIS experiences the same cluster of scatterers around that RIS so that the reflected signals are located in the same time-delay window and can be beamformed by the RIS. Therefore, the reflected channel provided by each RIS is also modeled by a one-tap channel.

the UEs in other cells $\rho_{R_{2,i,j}} \in \mathbb{C}$ are modeled as experiencing NLoS propagation. Specifically, we assume that the LoS links have a Rician fading and a path loss exponent $\alpha_{\text{LoS}} = 3$. We assume that the NLoS links experience a Rayleigh fading and a path loss exponent $\alpha_{\text{NLoS}} = 4$. Furthermore, we assume half-wavelength spacing for both transceivers and RISs, so that the fading variables of the direct links ρ_{D_i} and that of the reflected links $\rho_{R_{1,i,j}}^{(m)}$ and $\rho_{R_{2,i,j}}^{(m)}$ can be assumed independent [44, Corollary 1]. The mutual coupling between RIS elements is neglected in this work.

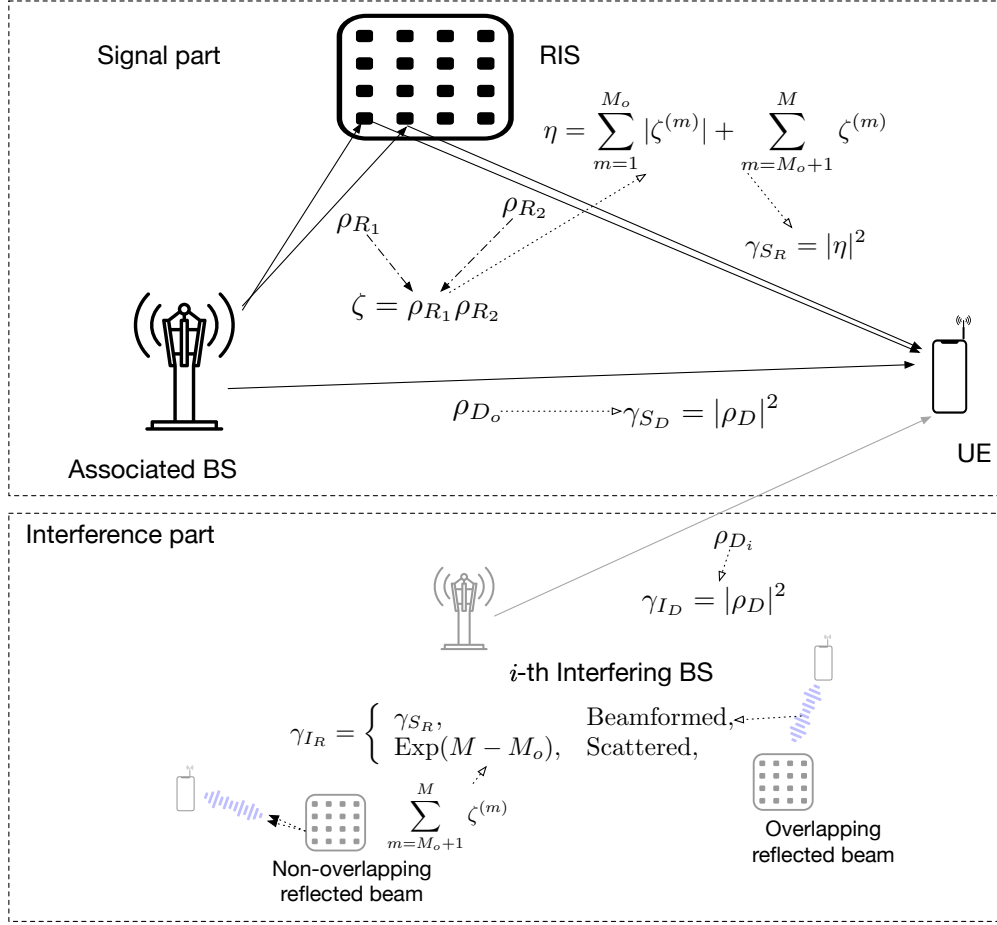


Fig. 2: An illustrative guide to the relationship of mathematical symbols, providing an overview of their interactions

For all links, we characterize the fading power of both the direct signal (denoted by γ_{S_D}) and the reflected signal (denoted by γ_{S_R}). Similarly, we analyze the fading power of the direct interference (denoted by γ_{I_D}) and the reflected interference (denoted by γ_{I_R}). The relationships between the fading notation used in this section are summarized in Fig. 2. In this chart, ρ denotes the small-scale fading experienced by a link. Since a reflected link consists of two links, the arrow from ρ to $\zeta \in \mathbb{C}$ characterizes $\zeta = \rho_{R_1} \rho_{R_2}$, as the small-scale fading experienced by the signal reflected by a RIS element. In turn, the arrow from ζ to $\eta \in \mathbb{C}$ represents the RIS reflection mechanism (see below) comprising two components: a coherent signal superposition caused by the RIS beamforming, and a non-coherent signal superposition arising from the RIS scattering.

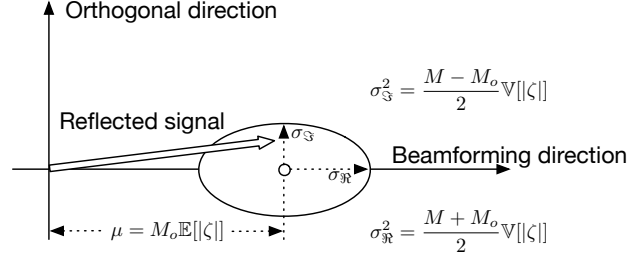


Fig. 3: Signal reflected from a RIS contains a beamformed part (approximated by real non-central Gaussian) and a scattered part (approximated by circular complex Gaussian).

Recall that the direct signals experience independent Rayleigh fading, thus we have

Lemma 1. *The powers of fading of both the direct signal $|\rho_{D_o}|^2$ and the direct interference $|\rho_{D_i}|^2$ follow a standard exponential distribution [36], denoted by $\gamma_{S_{D_o}} \sim \text{Exp}(1)$ and $\gamma_{S_{D_i}} \sim \text{Exp}(1)$.*

The characteristic of the reflected signal from each RIS depends on configuration. Since RISs are deployed at the system level to serve multiple UEs, we assume that every RIS associated with the typical UE allocates a batch of M_o RIS elements to perform beamforming to the typical UE. The other elements associated with the other UEs in the same cell simultaneously scatter the intended signal to the typical UE. This parameter will be discussed below.

We discuss the configuration of RIS for performing batched beamforming. A batch of M_o elements in the j^{th} RIS of the cluster ϕ_o performs beamforming towards the typical UE. The configuration profile $\Theta_{\mathbf{y}_{o,j}}$ in Eq. (1) of the RIS $\mathbf{y}_{o,j}$ is obtained batch-wise. Define the phase shifts of the reflected links as the phases of the fading $\theta_{R_{1,o,j}}^{(m)} = \angle(\rho_{R_{1,o,j}}^{(m)})$ and $\theta_{R_{2,o,j}}^{(m)} = \angle(\rho_{R_{2,o,j}}^{(m)})$. To perform the beamforming via phase alignment, the phase shift configuration for the batch associated with the typical UE is given by

$$\theta_{\mathbf{y}_{o,j}}^{(m)} = \theta_{R_{1,o,j}}^{(1)} + \theta_{R_{2,o,j}}^{(1)} - \left(\theta_{R_{1,o,j}}^{(m)} + \theta_{R_{2,o,j}}^{(m)} \right), \quad 1 < m < M_o, \quad (7)$$

where we assume the indices for the elements of the batch for the typical UE start from 1, without loss of generality. This configuration allows the reflected beam to arrive at the receiver in phase by setting the phase shift of the reflected signal from the m^{th} element as the reference phase. Here, $\zeta = \rho_{R_1} \rho_{R_2}$ is the reflected signal from one RIS element. Its mean and variance are given in Appendix A. The beamformed component of the reflected signal, as the result of in-phase signal superposition, is the sum of M_o i.i.d. random variables distributed as $|\zeta|$. The remaining elements in this RIS are allocated to other UEs in the cell but also scatter the signal, introducing the scattered component. The gain from the scattered signal is the sum of $M - M_o$ i.i.d. variables distributed like ζ . Consider the beamformed phase-shift as the reference phase of the received signal from the RIS, $\eta_{o,j} \in \mathbb{C}$ denotes the signal reflected by one RIS when the received signal is normalized by pathloss, given by

$$\eta_{o,j} = \sum_{m=1}^{M_o} |\zeta^{(m)}| + \sum_{m=M_o+1}^M \zeta^{(m)}, \quad (8)$$

where $\eta_{o,j}$ is aligned to the direction of the beamformed signal. Here, since both M_o and M are assumed large, thanks to the central limit theorem, we can approximate $\sum_{m=1}^{M_o} |\zeta^{(m)}|$ by a one-dimensional non-central Gaussian random variable $\mathcal{N}(M_o \mathbb{E}[|\zeta|], M_o \mathbb{V}[|\zeta|])$ and $\sum_{m=M_o+1}^M \zeta^{(m)}$ by a circular complex Gaussian random variable $\mathcal{CN}(0, (M - M_o) \mathbb{V}[|\zeta|])$. A circular Gaussian random variable can be decomposed into two components: one aligned with the beamformed signal and another orthogonal to it, as shown in Fig. 3. Then, the real part of $\eta_{o,j}$ is expressed by $\Re[\eta_{o,j}] \approx \mathcal{N}(\mu, \sigma_{\Re}^2)$, where $\mu = M_o \mathbb{E}[|\zeta|]$ and $\sigma_{\Re}^2 = \frac{M+M_o}{2} \mathbb{V}[|\zeta|]$. The imaginary part is $\Im[\eta_{o,j}] \approx \mathcal{N}(0, \sigma_{\Im}^2)$, where $\sigma_{\Im}^2 = \frac{M-M_o}{2} \mathbb{V}[|\zeta|]$.

Lemma 2. *Recall that the fading of reflected signal $\gamma_{S_R} = |\eta_{o,j}|^2, \forall j \in \mathcal{J}_o$. The Laplace transform of the power of the fading of the reflected signal from a RIS is*

$$\mathcal{L}_{\gamma_{S_R}}(s) = \frac{\exp\left(-\frac{\mu^2 s}{1+2s\sigma_{\Re}^2}\right)}{\sqrt{(1+2s\sigma_{\Re}^2)(1+2s\sigma_{\Im}^2)}}, \quad s > -\frac{1}{2\sigma_{\Re}^2}. \quad (9)$$

Proof. As the result of the sum of the power of the real part, as an independent non-central Gaussian, which is the power of the imaginary part, modeled as another independent central Gaussian distribution, the fading power of the reflected beam is a generalized non-central chi-square distribution, The corresponding Laplace transform is given by the product of the Laplace transform of the two independent Chi-Square random variables, given by

$$\mathcal{L}_{\gamma_{S_R}}(s) = \mathcal{L}_{\chi^2(\mu, \sigma_{\Re}^2)}(s) \mathcal{L}_{\chi^2(0, \sigma_{\Im}^2)}(s), \quad (10)$$

where $\chi^2(\mu, \sigma^2)$ denotes the power of the corresponding normal distribution $\mathcal{N}(\mu, \sigma^2)$. The expression of the Laplace transform of the chi-square distribution can be found in [45]. The result follows. \square

The fading of the reflected interference from other cells, i.e., $\eta_{i,j}$, fading depends on whether the typical UE is located within the reflected beam. Let ϑ_{beam} denote the beamwidth of a reflected beam. In [46], the authors demonstrate that the beamwidth of the reflected signal is inversely proportional to the number of RIS elements. Their numerical results validate a beamwidth of around 1-2 degrees for a 64-element RIS. Based on their analysis and verified data, for the setup with hundreds of elements, we can conservatively expect the beamwidth to be approximated by $\vartheta_{\text{beam}} = \frac{180^\circ}{M_o}$, where M_o is the number of batch elements forming that beam. The probability when an arbitrarily directed interfering beam overlaps the typical UE is determined by the beamwidth divided by the total angular region 360° , as illustrated in Fig. 2. If the typical UE is located within the interfering beam, the fading characterization is the same as the fading $|\eta|^2$ for the reflected signal. Otherwise, only the scattered component $\sum_{m=M_o+1}^M \zeta^{(m)}$ reaches the typical UE, and the power of the fading follows an exponential distribution with the scale $(M - M_o)$. We have hence

Lemma 3. *Recall that γ_{I_R} denotes the fading power of the reflected interference. The distribution can be characterized by*

$$\gamma_{I_R} = \begin{cases} \gamma_{S_R}, & \text{with probability } \frac{\vartheta_{\text{beam}}}{360^\circ}, \\ \text{Exp}(M - M_o), & \text{with probability } 1 - \frac{\vartheta_{\text{beam}}}{360^\circ}, \end{cases} \quad (11)$$

where $\text{Exp}(M - M_o)$ refers to the exponential distribution with the scale parameter $(M - M_o)$.

Proof. When the interfering beam directly affects the typical UE, the UE experiences fading similar to Eq. (8). Otherwise, the beam is directed elsewhere, and the UE only receives the scattered component, which is approximated by a circular complex Gaussian random variable $\mathcal{CN}(0, (M - M_o)\mathbb{V}[|\zeta|])$. The power of this scattered component follows an exponential distribution. \square

These two cases will be used to characterize the total interference when we consider the spatial randomness. It is worthwhile mentioning that the proportion of the scattered energy is most often negligible compared to the direct link and the reflected beams under certain conditions [17]. This is because the multiplicative pathloss is much higher than that of the direct interference. Unlike the beamformed reflected signal, the high multiplicative pathloss is not compensated by the beamforming mechanism. This quantitative relationship will be investigated and confirmed in the section on numerical results.

III. MODELING RISS AS MATÉRN CLUSTER PROCESSES

In this section, we focus on investigating a BS-centric specialization, where RISs are strategically positioned around BSs and modeled as MCP. The same procedures for signal processing and performance assessment will allow us to explore different deployment strategies in the next section.

A. MCP model

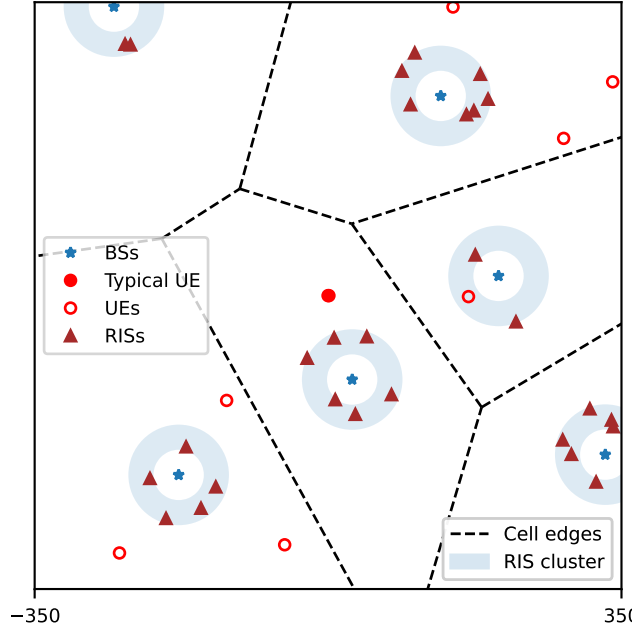


Fig. 4: A MCP model of a RIS-assisted cellular network

This BS-centric model is motivated by the assumption that the RISs are directly controlled by their associated BS via a dedicated control channel. To model the geometry of the RIS deployment, we examine two spatial constraints. Due to the physical limitations of both BSs and RISs, we introduce a minimum separation distance R_{in} between

the BS and the RISs. This minimum distance constraint prevents the case where the BS and RIS are too close, which would invalidate the far-field channel model. We also define a maximal separation distance R_{out} between the BS and the RISs, guaranteeing that the RISs can receive and reflect sufficient energy from the associated BS.

The locations of BSs and RISs are thus modeled as an MCP consisting of a *mother point process* and a *daughter point process*, as shown in Fig. 4. The mother point process of the MCP coincides with the locations of BSs that are modeled as the homogeneous PPP Φ_{BS} . The *daughter point process*, conditioned on Φ_{BS} , are PPPs with the density λ_{RIS} . Each cluster ϕ_i has support on the ring $\mathbb{D}_{\mathbf{x}_i}(R_{\text{in}}, R_{\text{out}})$, i.e., the ring centered at \mathbf{x}_i with an inner radius R_{in} and an outer radius R_{out} . More precisely, the total number of points of ϕ_i is Poisson distributed with parameter $\lambda_{\text{RIS}}\pi(R_{\text{out}}^2 - R_{\text{in}}^2)$ and every point of ϕ_i follows the probability density function (PDF),

$$f_{\text{MCP}}(\mathbf{y}) = \begin{cases} \frac{1}{\pi(R_{\text{out}}^2 - R_{\text{in}}^2)} & \text{if } \mathbf{y} \in \mathbb{D}_{\mathbf{x}_i}(R_{\text{out}}, R_{\text{in}}), \\ 0 & \text{otherwise.} \end{cases} \quad (12)$$

Note that this model assumes that RISs are positioned closer to the associated BS than non-associated ones. To ensure this, we should restrict the BS density within a range where the inter-BS distance is significantly larger than twice the outer radius of the clusters. We take here $2R_{\text{out}} \ll \frac{1}{2\sqrt{\lambda_{\text{BS}}}}$. In RIS-assisted cellular networks that do not satisfy this restriction, signal reflections from non-associated clusters may become significant and must be incorporated into the model.

B. Signal Processing

Prior to signal processing, we consider the ideal scenario where the typical UE has perfect channel state information (CSI) $Z_o[n]$, $n \in [N_c]$. This is achieved by the associated BS transmitting pilot signals on a dedicated channel, allowing the UE to perform channel estimation. However, the typical UE is agnostic to $Z_i[n]$, $n \in [N_c]$.

It is worthwhile mentioning that signals and channels can be analyzed in both the time and frequency domains. This duality means that modulating a signal in one domain will be reflected by its representation in the other domain. In an OFDM system, we assume the carrier of a total bandwidth B to be equally divided into N_s subcarriers. A codeword of N_s symbols, denoted by $\mathfrak{s}_i[k]$, $k \in [N_s]$, is modulated on the BS at \mathbf{x}_i over the OFDM subcarriers. This codeword is transmitted as a symbol sequence in the time domain $s_i[n]$, $n \in [N_s]$, obtained by the inverse discrete Fourier transform (IDFT) of the codeword in the frequency domain

$$s_i[n] = \frac{1}{\sqrt{N_s}} \sum_{k=0}^{N_s-1} \mathfrak{s}_i[k] \exp\left(\frac{i2\pi kn}{N_s}\right). \quad (13)$$

For the channel $Z_i[n]$, we use $\mathcal{Z}_i[k]$ to denote the channels in the frequency domain. Here, we use n and k to index the symbol block in the time and frequency domain, respectively.

Recall that N_c is the time dispersion duration of the discrete channel. In the OFDM system, the symbol block is appended with a cyclic prefix of length $N_c - 1$ to mitigate inter-symbol interference (ISI). We further assume that $N_s \gg N_c$, and thus the frequency response of individual subcarriers is flat and the impact of the cyclic prefix is negligible and we neglect it⁴ [16]. As mentioned earlier, $s_o[n] \in \mathbb{C}$ denotes the signal symbol blocks w.r.t. the

⁴Note that the OFDM technique appends the cyclic prefix of length $N_c - 1$ to the symbol block consisting of the end of the sequence, and then removes the last $N_c - 1$ received symbols at the receiver side. As a result, the length of the symbol block in the time domain remains N_s .

typical UE. In this cellular network, the remaining BSs send signals $s_i[n]$ over the same frequency band, creating system-level interference. Let $\bar{s}_o[n], n \in [N_s]$ define the signal received at the typical UE, given by

$$\bar{s}_o[n] = Z_o[n] \circledast s_o[n] + \sum_{i \neq o} \left(Z_i[n] \circledast s_i[n] \right) + w[n], \quad \forall n \in [N_s], \quad (14)$$

where \circledast is the circular convolution operation [16]. We recall that $Z_o[n]$ is the channel of the BS to which the typical UE is associated, defined in Eq. (2). The first term in Eq (14) will be called signal and the second interference. Here, $w[n]$ denotes the white Gaussian noise. In the following, we discuss its impact on the signal and the interference separately.

In the next section, we will discuss the network performance using the Shannon channel capacity. The maximum number of nats per symbol that can be reliably communicated is a function of SINR,

$$\log \left(1 + \frac{Q_S}{Q_I + \sigma_w^2} \right), \quad (15)$$

where Q_S is the average signal power of the received codeword, whereas Q_I and σ_w^2 are the interference and noise power, respectively. In this work, we assume that the channel coding is applied jointly across subcarriers, for which the average received power for the codewords depends on the channel gain given in Lemma 4. Remark that the channel gains of individual subcarriers are not identical for the frequency-selective channel. This variation can lead to a higher error probability for some codewords than others in the codebook based on the average power constraints. However, the decoding error depends on the efficiency and the asymptotic behavior of error correction codes. In practice, when the channel knowledge of the frequency-selective channel is available at the transmitter side, further optimization for channel coding is possible by allocating the available power across subcarriers using the waterfilling algorithm. This allows the practical channel capacity to be higher than the evaluated capacity given in Eq. (15).

Consider a symbol transmitted over the k^{th} subcarrier, denoted by $\mathfrak{s}_o[k], k \in [N_s]$, the signal power defined in terms of average energy per symbol time is

$$\begin{aligned} \mathbb{E}[\mathfrak{s}_o^2[k]] &= \mathbb{E} \left[\left| \frac{1}{\sqrt{N_s}} \sum_{n=0}^{N_s-1} s_o[n] \exp \left(\frac{-i2\pi kn}{N_s} \right) \right|^2 \right] \\ &= \frac{1}{N_s} \mathbb{E} \left[\left| \sum_{n=0}^{N_s-1} s_o[n] \exp \left(\frac{-i2\pi kn}{N_s} \right) \right|^2 \right] \stackrel{(a)}{=} P_0, \end{aligned} \quad (16)$$

where (a) follows from the fact that, in most modulation schemes, such as QPSK or QAM, the transmitted signals $s_i[n], n \in [N_s]$ are i.i.d. random variables with zero mean and variance P_0 . Note that the transmission of this symbol $\mathfrak{s}_o[k]$ over one OFDM subcarrier of bandwidth $\frac{B}{N_s}$, as shown in Eq. (13), takes N_s symbol times. Hence, the transmission power of the subcarrier is $\frac{P_0}{N_s}$.

To recover the encoded codeword $\mathfrak{s}_o[k], k \in [N_s]$, the receiver applies the discrete Fourier transform to the received signal and interference $\bar{s}_o[n]$ in Eq. (14), expressed as

$$\bar{\mathfrak{s}}_o[k] = \mathcal{Z}_o[k] \cdot \mathfrak{s}_o[k] + \sum_{i \neq o} \left(\mathcal{Z}_i[k] \cdot \mathfrak{s}_i[k] \right) + w[k], \quad \forall k \in [N_s]. \quad (17)$$

Here, $\mathcal{Z}_o[k]$, $k \in [N_s]$ denotes the channel gains over subcarriers, given by $\mathcal{Z}_o[k] = \sum_{n=0}^{N_s-1} Z_o[n] \exp\left(\frac{-i2\pi nk}{N_s}\right)$, $k \in [N_s]$, where we append zeros $Z_o[n] = 0$ for all $n \in \{N_c, \dots, N_s - 1\}$. Note that the channel gain over subcarriers is the unitary version of DFT scaled by $\sqrt{N_s}$, ensuring that the transformed value is equal to the frequency response of the channel [16, Eq. (3.138)]⁵. The channel gains for the interference $\mathcal{Z}_i[k]$, $k \in [N_s]$ are defined in the same way.

Since the received signal over the k^{th} subcarrier is $\mathcal{Z}_o[k] \cdot \mathfrak{s}_o[k]$, the received signal power on that subcarrier is $|\mathcal{Z}_o[k]|^2 \frac{P_0}{N_s}$. The numerator of the SINR in Eq. (15) is hence given by

$$Q_S = \sum_{k=0}^{N_s-1} |\mathcal{Z}_o[k]|^2 \frac{P_0}{N_s} := \hat{h}_o^2 P_0, \quad (18)$$

where $\hat{h}_o^2 = \frac{1}{N_s} \sum_{k=0}^{N_s-1} |\mathcal{Z}_o[k]|^2$. We have

Lemma 4. *Under the foregoing assumptions, the scaling factor caused by the RIS-assisted channel for the OFDM signals is given by*

$$\hat{h}_o^2 = \gamma_{S_{D_o}} g(\|\mathbf{x}_o\|) + \sum_{j \in \mathcal{J}_o} \gamma_{S_{R_o,j}} G(\mathbf{x}_{o,j}, \mathbf{y}_{o,j}). \quad (19)$$

Proof. Thanks to Parseval's theorem [47], the power of the channel gain in the frequency domain equals the power of the multipath taps in the time domain,

$$\begin{aligned} \hat{h}_o^2 &= \frac{1}{N_s} \sum_{n=0}^{N_s-1} |\mathcal{Z}_o[k]|^2 = \sum_{n=0}^{N_s-1} |Z_o[n]|^2 \\ &\stackrel{(a)}{=} |h_{D_o} \delta(n - n_{D_o})|^2 + \sum_{j \in \mathcal{J}_o} |h_{R_o,j} \delta(n - n_{R_o,j})|^2 \\ &\stackrel{(b)}{=} |h_{D_o}|^2 + \sum_{j \in \mathcal{J}_o} |h_{R_o,j}|^2 \\ &\stackrel{(c)}{=} \gamma_{S_{D_o}} g(\|\mathbf{x}_o\|) + \sum_{j \in \mathcal{J}_o} \gamma_{S_{R_o,j}} G(\mathbf{x}_{o,j}, \mathbf{y}_{o,j}), \end{aligned} \quad (20)$$

where (a) holds when the delays of the paths from the BS and the RISs are all different; (b) follows from the fact that the amplitude of the discrete Dirac function is one; (c) follows from the Lemma 1 and Lemma 2 in Subsection II-C. \square

As a result, OFDM can exploit the multipath diversity gain by mapping the time dispersion of the channel into the frequency domain.

Next, we discuss the fading distribution of the processed interference. We assume that RISs in the neighboring cells do not intentionally direct their interfering beams toward the typical UE, since they are primarily responsible for serving UEs within their designated cells. To characterize the reflected interference, the reflected interfering beams have random direction and there is a small probability that these beams overlap with the typical UE. If the

⁵Readers may be curious why the transform between time and frequency domain for the channel gain needs to be scaled by $\sqrt{N_s}$, but that of the signal power in terms of energy per symbol time is not scaled. This is because in discussing N_s symbols over the N_s subcarriers, the transform of the channel gain considers the scaling effect of a unit symbol time, but the transform of the symbol power considers the N_s symbol times.

reflected beam does not overlap, the interference from that RIS is mainly the scattering part. This probabilistic fading is discussed in Lemma 3. The interfering channel is given by

$$Z_i[n] = h_{D_i} \delta[n - n_{D_i}] + \sum_{j \in \mathcal{J}_i} h_{R_{i,j}} \delta[n - n_{R_{i,j}}]. \quad (21)$$

The same analysis for processing the signal, given in Eq. (18), applies to processing the interference, too. We define $\hat{h}_i^2 \in \mathbb{R}$ as the effective channel gain for the interference from the i^{th} interferer, given by

$$\hat{h}_i^2 = \frac{1}{N_s} \left[\sum_{k=0}^{N_s-1} |Z_i[k]|^2 \right] = |Z_i[k]|^2. \quad (22)$$

Following the same analysis in Lemma 4, the effective channel gain for the interference from the i^{th} BS is given by

$$\hat{h}_i^2 = \gamma_{I_{D_i}} g(\|\mathbf{x}_i\|) + \sum_{j \in \mathcal{J}_i} \gamma_{I_{R_{i,j}}} G(\mathbf{x}_{i,j}, \mathbf{y}_{i,j}), \quad (23)$$

where both $\gamma_{I_{D_i}}$ and $\gamma_{I_{R_{i,j}}}$ are given in Lemma 1 and Lemma 3, respectively. The noise term is independent of the BSs and RISs, and we denote the noise power as σ_w^2 .

C. Analysis of Coverage Probability and of Ergodic Rate

Next, we assess the coverage probability and the ergodic rate in a RIS-assisted cellular network. The coverage probability is defined as the probability that the SINR of the typical UE is larger than a target threshold $T > 0$. Conditioned on the distance from the associated BS to the typical UE $r = \|\mathbf{x}_o\|$, i.e., $P_c(T|r)$, then the coverage probability is $P_c(T|r) \triangleq \mathbb{P}(\text{SINR} \geq T|r)$, where SINR is defined by

$$\frac{\gamma_{S_D} P_0 g(r) + \sum_{j \in \mathcal{J}_o} \gamma_{S_{R_{o,j}}} P_0 G(\mathbf{x}_o, \mathbf{y}_{o,j})}{\sum_{i \neq o} (\gamma_{I_{D_i}} P_0 g(\|\mathbf{x}_i\|) + \sum_{j \in \mathcal{J}_i} \gamma_{I_{R_{i,j}}} P_0 G(\mathbf{x}_i, \mathbf{y}_{i,j})) + \sigma_w^2}. \quad (24)$$

Here, σ_w^2 is the power of the Gaussian noise. In the following, we introduce notations for manipulating expressions. To account for the two components of the signal power Q_S , we let the direct signal power be $Q_{S_D}(r) = \gamma_{S_D} P_0 g(r)$ and the reflected signal power be $Q_{S_R}(r) = \sum_{j \in \mathcal{J}_o} \gamma_{S_{R_{o,j}}} P_0 G(\mathbf{x}_o, \mathbf{y}_{o,j})$. The total interference power is $Q_I = \sum_{i \neq o} (\gamma_{I_{D_i}} P_0 g(\|\mathbf{x}_i\|) + \sum_{j \in \mathcal{J}_i} \gamma_{I_{R_{i,j}}} P_0 G(\mathbf{x}_i, \mathbf{y}_{i,j}))$. After manipulating the SINR components, the coverage probability can be expressed by

$$P_c(T|r) = \mathbb{P} \left[\frac{Q_{S_D}(r) + Q_{S_R}(r)}{Q_I(r) + \sigma_w^2} \geq T | r \right] = \mathbb{P} [Q_{S_D}(r) \geq T(Q_I(r) + \sigma_w^2) - Q_{S_R}(r) | r]. \quad (25)$$

Next, let

$$\Upsilon = T(Q_I(r) + \sigma_w^2) - Q_{S_R}(r). \quad (26)$$

Note that the probability distribution function for $Q_I(r)$ is defined over \mathbb{R}^+ because the power of interference is non-negative⁶. Similarly, the summed reflected signals $Q_{S_R}(r)$ is defined over \mathbb{R}^+ too. By definition, the random variable Υ is the difference between the above two non-negative random variables, which is defined over \mathbb{R} . Hence,

⁶Notice that in the domain of $Q_I(r)$, which is \mathbb{R}^+ , the unilateral Laplace transform $\mathcal{L}_{Q_I(r)}(s)$ and the bilateral Laplace transform $\mathcal{B}_{Q_I(r)}(s)$ are the same.

we use the bilateral Laplace transform $\mathcal{B}_\Upsilon(s)$ to characterize the Υ . The bilateral Laplace transform $\mathcal{B}_\Upsilon(s)$ is obtained by the product of the Laplace transforms of $\mathcal{B}_{TQ_I(r)}(s)$ and that of $\mathcal{B}_{-Q_{S_R}(r)}(s)$ ⁷,

$$\mathcal{B}_\Upsilon(s) = \mathcal{B}_{TQ_I(r)}(s)\mathcal{B}_{T\sigma_w^2}(s)\mathcal{B}_{-Q_{S_R}(r)}(s), \quad (27)$$

since the random variables $TQ_I(r)$ and $Q_{S_R}(r)$ are independent. The power of the Gaussian noise σ_w^2 is constant, thus $\mathcal{B}_{T\sigma_w^2}(s)$ is also a constant. We then discuss $TQ_I(r)$ and $Q_{S_R}(r)$ separately.

We first calculate the Laplace transform of the PDF for the total interference power $Q_I(r)$, which accounts for three types of randomness: 1) the randomness of interfering signals; 2) the randomness of the channel fading $\gamma_{I_{D_i}}$ and $\gamma_{I_{R_i,j}}$; 3) the network geometry. We have

Lemma 5. *The Laplace transform of the distribution function of the interference power level, given that the typical UE is placed at $r = \|\mathbf{x}_o\|$ meters away from its associated BS, is equal to*

$$\mathcal{B}_{TQ_I(r)}(s) = \exp\left(-2\pi\lambda_{\text{BS}} \int_r^\infty x \left(1 - \mathcal{L}_{TQ_c(x)}(s)\right) dx\right), \quad (28)$$

where $Q_c(x)$ denotes the interference power from a cluster with the distance from the BS in that cell to the typical UE $x = \|\mathbf{x}\|$. The Laplace transform of the distribution of the scaled interference power $TQ_c(x)$ is given by

$$\begin{aligned} \mathcal{L}_{TQ_c(x)}(s) = & \\ & \frac{e^{\left(\frac{\vartheta_{\text{beam}}}{2\pi} \lambda_{\text{RIS}} \int_0^{2\pi} \int_{R_{\text{in}}}^{R_{\text{out}}} \left(1 - \mathcal{L}_{\gamma_{S_R}}(sP_0T\mathcal{G}(x,y,\psi))\right) dyd\theta\right)}}{1 + sP_0Tg(x)} \times e^{\left(\left(1 - \frac{\vartheta_{\text{beam}}}{2\pi}\right) \lambda_{\text{RIS}} \int_0^{2\pi} \int_{R_{\text{in}}}^{R_{\text{out}}} \left(1 - \frac{1}{1+s(M-M_o)P_0T\mathcal{G}(x,y,\psi)}\right) dyd\theta\right)}. \end{aligned} \quad (29)$$

In Eq. (29), we use the notation with

$$\mathcal{G}(x, y, \psi) = g(y)g(\sqrt{x^2 + y^2 - 2xy \cos \psi}), \quad (30)$$

for $x, y, \in \mathbb{R}$, $\psi \in [0, 2\pi)$, where $\|\mathbf{y}\| = y$ and $\|\mathbf{x} - \mathbf{y}\| = \sqrt{x^2 + y^2 - 2xy \cos \psi}$, and ψ is the angle between the link from the BS to the UE and that from the BS to the RIS.

Proof. See Appendix B. □

For the aggregated power of the reflected signal by RISs, there are two types of randomness: 1) the randomness of the power of the channel fading γ_R ; 2) the randomness of the spatial deployment of RISs ϕ_o . We have

⁷In functional analysis, the Laplace transform of a function f with positive support usually refers to the unilateral Laplace transform, given by

$$\mathcal{L}_f(s) = \int_0^\infty f(t)e^{-st} dt, \quad t \geq 0.$$

The Laplace transform can be extended to functions with support on the whole real line via the bilateral Laplace transform, given by

$$\mathcal{B}_f(s) = \int_{-\infty}^\infty f(t)e^{-st} dt, \quad t \in \mathbb{R},$$

under the condition that the integral exists. In probability theory, the Laplace transform of a random variable X with density function f_X is defined by $\mathbb{E}[e^{-sX}] = \int_{-\infty}^\infty f_X(t)e^{-st} dt$, where the range of integration is the support of the random variable X . Specifically, the Laplace transform is defined by $\mathcal{L}_X(s)$ when X is a non-negative random variable and by $\mathcal{B}_X(s)$ when X is defined over the entire real axis.

Lemma 6. *The Laplace transform of the PDF of the aggregated power of the reflected signal, given that the typical UE is placed at $r = \|\mathbf{x}_o\|$ meters away from its associated BS, is given by*

$$\begin{aligned} & \mathcal{B}_{-Q_{S_R}(r)}(s) \\ &= \mathbb{E}_{\phi_o, \gamma_{S_{R_o,j}}} \left[\exp \left(s \sum_{\mathbf{y}_{o,j} \in \phi_o} \gamma_{S_{R_o,j}} P_0 G(\mathbf{x}_o, \mathbf{y}_{o,j}) \right) \right] \\ & \stackrel{(a)}{=} e \left(-\lambda_{\text{RIS}} \int_{R_{\text{in}}}^{R_{\text{out}}} \int_0^{2\pi} y \left(1 - \mathcal{L}_{\gamma_{S_R}}(-s P_0 \mathcal{G}(r, y, \psi)) \right) d\psi dy \right), \end{aligned} \quad (31)$$

where (a) follows from the probability generating function (PGFL) of ϕ_o is a PPP defined over the cluster support $\mathbb{D}_{\mathbf{x}_o}(R_{\text{in}}, R_{\text{out}})$. Specifically, we discuss the region of convergence for s in Appendix C.

Next, we decompose $\Upsilon = \Upsilon^+ + \Upsilon^-$, where $\Upsilon^+ = \max\{0, \Upsilon\}$ and $\Upsilon^- = \min\{0, \Upsilon\}$ to prepare for computing the coverage probability. We have the following theorem:

Theorem 1. *The Laplace transform of the positive part of a random variable can be derived from its bilateral Laplace transform via the formula*

$$\mathcal{L}_{\Upsilon^+}(s) = \frac{1}{2\pi i} \int_{-\infty}^{\infty} \left(\mathcal{B}_{\Upsilon}(s - u) - \mathcal{B}_{\Upsilon}(-u) \right) \frac{du}{u} + \frac{1}{2} \left(1 + \mathcal{B}_{\Upsilon}(s) \right) - \mathcal{B}_{\mathcal{B}_{\Upsilon}(s)/s}^{-1}(0), \quad (32)$$

where $\int_{-\infty}^{\infty} \frac{du}{u}$ is understood in the sense of Cauchy principal-value, that is $\int_{-\infty}^{\infty} = \lim_{\epsilon \downarrow 0} \int_{-\infty}^{-\epsilon} + \int_{\epsilon}^{\infty}$, and $\mathcal{B}^{-1}(0)$ denotes the inverse Laplace transform evaluated at 0, with the Bromwich integral taken over a vertical contour in the convergence domain discussed in Appendix C.

Proof. Please refer to Appendix D. □

Corollary 1. *Applying the Leibniz integral rule to Eq (32), we can directly obtain the k -th derivatives $\mathcal{L}_{\Upsilon^+}^{(k)}(s)$,*

$$\mathcal{L}_{\Upsilon^+}^{(k)}(s) = \frac{1}{2\pi i} \int_{-\infty}^{\infty} \mathcal{B}_{\Upsilon}^{(k)}(s - u) \frac{du}{u} + \frac{1}{2} \mathcal{B}_{\Upsilon}^{(k)}(s), \quad n > 0. \quad (33)$$

Lemma 7. *When RISs are configured as batched beamformers, the coverage probability for the communication threshold T is given by*

$$P_c(T|r) = \mathcal{L}_{\Upsilon^+} \left(\frac{1}{P_0 g(r)} \right) + \mathcal{B}_{\mathcal{B}_{\Upsilon}(s)/s}^{-1}(0) \quad (34)$$

Proof. We first compute the coverage probability conditioned on r , i.e., $\mathbb{P}(T|r)$ in Eq. (25), given by

$$\begin{aligned} & \mathbb{P} \left[\gamma_{S_D} P_0 g(r) \geq \Upsilon | r \right] = \mathbb{P} \left[\gamma_{S_D} \geq \frac{\Upsilon}{P_0 g(r)} | r \right] \\ & \stackrel{(a)}{=} \int_0^{\infty} e^{-\frac{v}{P_0 g(r)}} f_{\Upsilon}(v) dv + \int_{-\infty}^0 f_{\Upsilon}(v) dv \\ & \stackrel{(c)}{=} \mathcal{L}_{\Upsilon^+} \left(\frac{1}{P_0 g(r)} \right) + \mathbb{P}[\Upsilon < 0], \end{aligned} \quad (35)$$

where (a) follows from the complementary cumulative distribution function (CCDF) of the exponential distribution, defined as $\bar{F}_{\text{Exp}(1)}(t) = \int_t^{\infty} e^{-t} dt$. Here, the dummy variable v is integrated over the positive axis since the fading γ_{S_D} is defined over the \mathbb{R}^+ ; (b) follows from the definition of the Laplace transform of $\mathcal{L}_{\Upsilon^+}(s) =$

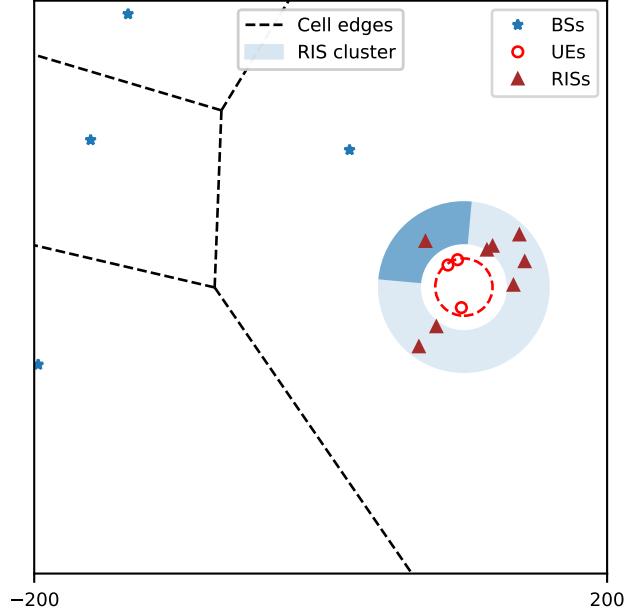


Fig. 5: RISs deployed to serve UEs in the coverage hole

$\int_{v>0} e^{-sv} f_{\Upsilon^+}(v) dv$, with the argument as $s = \frac{1}{P_{0g}(r)}$. Finally, plugging $\mathbb{P}[\Upsilon < 0] = \mathcal{B}_{\mathcal{B}_{\Upsilon}(s)/s}^{-1}(0)$, we obtain the expression. \square

Ergodic rate: Based on the coverage probability $P_c(T|r)$, we can further obtain the ergodic rate defined by the adaptive Shannon rate, given by [37]

$$\tau(r) \triangleq \mathbb{E}[\log(1 + \text{SINR})] = \int_0^\infty \frac{P_c(t|r)}{t+1} dt. \quad (36)$$

It is important to note that the ergodic rate in this context refers to the average performance across random UEs, RIS deployment, random link fading, and interference. However, the distance between the BS and the UE is specified by the fixed parameter r . This is because several physical constraints will influence the set of UEs that are strategically associated with RISs.

IV. EXTENSIONS AND VARIANTS

The proposed framework offers a modular design, where the reflected signals and the interference defined in Section II are first represented by Laplace transforms and then combined to derive the performance metrics. The aim of this section is to demonstrate the framework's adaptability and versatility through the exploration of various scenarios and deployment strategies.

We investigate the deployment of multiple RISs to address coverage holes caused by urban buildings that can block the direct signal. As shown in Fig. 5, the RISs are deployed in a cluster ring surrounding a coverage hole, parameterized by $\mathbb{D}_r(R_{\text{in}}, R_{\text{out}})$, where r denotes the distance between the BS to the center of the coverage hole. The RISs will reflect signals toward UEs located within the coverage hole, when assuming configuration similar to that defined in the MCP model. Let a circle of radius $R_{\text{CH}} < R_{\text{in}}$ model the coverage hole in which the typical

UE, located at \mathbf{u} , can be selected. This selection ensures that the UEs are located in the far-field region of the RISs. We adopt the MCP model by placing the RIS ring around the coverage hole, creating a UE-centric approach. We will discuss how this example can extend the MCP model in three directions.

a) Variants of deployment area: Analyzing this UE-centric model is efficient due to its symmetry with the BS-centric model investigated in the previous section. Specifically, the signal propagation paths, BS-RIS-UE in the BS-centric model and UE-RIS-BS in the UE-centric model are essentially mirrored. This allows one to directly apply the analysis developed for the BS-centric model, with one adjustment on distance calculations $\mathcal{G}(r, y, \psi)$ in Lemma 6. The new distance calculations will account for the two segments of the reflected path in the new setup: BS-RIS and RIS-UE, given by

$$\mathbf{g}(\mathbf{x}_o, \mathbf{y}_{o,j}, \mathbf{u}) = g(\|\mathbf{x}_o - \mathbf{y}_{o,j}\|)g(\|\mathbf{y}_{o,j} - \mathbf{u}\|). \quad (37)$$

To further optimize signal coverage, we can extend the deployment beyond a ring shape. This allows us to prioritize signal assistance for UEs in specific areas around the coverage hole. To model this variant, we consider deploying RIS in a wedge-shaped area with an angle spanning a sector of the ring $\psi \in [-\frac{\varpi}{2}, \frac{\varpi}{2}]$, where ϖ defines the angle of the wedge sector, determined by the environment constraint. This modeling requires one to integrate over the area defining the wedge instead of the ring-shape in Lemma 6, which will be later materialized in Eq. (38).

Remark that the possible shape of RIS support is flexible too. For instance, in a street canyon scenario, a narrow vertical strip deployment of RIS units would be most effective. Alternatively, for deploying RISs on top of buildings, a rectangular RIS deployment on the rooftop can be more practical. For complex deployments, multiple RIS clusters can be defined within a single cell to address intricate coverage needs. This flexibility extends beyond 2D modeling, allowing researchers to model linear structures like streets (1D) or incorporate building height for 3D skyscraper scenarios.

b) Variants of PP: Different PPs can be used to model the locations of RISs. For example, we can consider models by specifying the exact number of RISs in the area. This can be modeled using the binomial point process (BPP), where $N_{\text{RIS}} \in \mathbb{N}^+$ represents the number of deployed RISs. Recall that Lemma 6 characterizes the aggregated reflected signal using the Laplace transform of PPP. To incorporate the BPP model defined on the wedge-shaped area, the Laplace transform of the signal power from the associated RISs is given by

$$\mathcal{L}_{\phi_i}(s) = \left(\int_{R_{\text{in}}}^{R_{\text{out}}} \int_{-\frac{\varpi}{2}}^{\frac{\varpi}{2}} \mathcal{L}_{\gamma_{S_R}} \left(-sP_0 \mathbf{g}(\mathbf{x}_o, \mathbf{y}_{o,j}, \mathbf{u}) \right) d\psi dy \right)^{N_{\text{RIS}}} \quad (38)$$

Compared to Equation (31), Equation (38) gives the Laplace transform of the combined reflected signals for BPP. We observe that the only modifications to accommodate this variant consists in replacing the Laplace transform of the RIS PPP with that of BPP, and updating the integration area. Remark that deploying a single RIS can be regarded as a special case in the BPP model by setting $N_{\text{RIS}} = 1$.

c) Variants of blockage: When the links are severely blocked, some penalty coefficients C_D for direct links and C_R for reflected links are incurred. Then the SINR is replaced by

$$\frac{C_D Q_{S_D}(r) + C_R Q_{S_R}(r)}{Q_I(r) + \sigma_w^2} \geq T. \quad (39)$$

Using the same manipulation as in Eq. (25), the coverage probability can be expressed by $\mathbb{P}[C_D Q_{S_D}(r) \geq Q_I(r) + \sigma_w^2 - C_R Q_{S_R}(r)]$. Then the coverage probability can be evaluated in terms of the Laplace transform of $\frac{1}{C_D} \Upsilon(C_R) = \frac{1}{C_D} (Q_I(r) + \sigma_w^2 - C_R Q_{S_R}(r))$, which can further be written as the Laplace transform of Q_{S_R} . Following the scaling rule of Laplace transforms $f_{\Upsilon}(at) \leftrightarrow \frac{1}{a} \mathcal{B}(\frac{s}{a})$ [48], this evaluation can be easily updated.

It is important to note that this simplified blockage model serves as a foundation for exploring the role of RIS in obstructed environments. More complex scenarios can be built upon this framework by incorporating various statistical models that account for factors like propagation distance, environment type, and carrier frequency. Based on this framework, these additional models can be investigated for a more comprehensive understanding of the role of RIS.

d) Scenarios for future exploration of more use cases: To account for different channel conditions and antenna technologies, fading distribution can be refined given the specification. For example, replacing the Laplace transform of $\mathcal{L}_{\gamma_{S_R}}(s)$ in Lemma 6 can generalize the fading model to describe variants of the reflected link or different RIS configuration. Replacing the Laplace transform of γ_{I_D} and γ_{I_R} can further generalize the interference characteristics to cope with different scenarios and environment schemes. Moreover, extending the direct link beyond Rayleigh fading, for example, Nakagami-m fading, can be adapted by evaluating higher order derivatives of the Laplace transform given by Corollary 1 (see e.g. , [32]). Remark that all the above extensions discussed in this section are modular and can be performed independently for specific use cases. Our framework thus offers solutions for many more scenarios.

V. NUMERICAL RESULTS

This section presents results from both Monte Carlo simulation and analytical calculation. To understand the RIS-assisted cellular networks, we first study the overall interference behavior based on the MCP model and further analyze the impact of the MCP parameters. Then, we evaluate the extended variant using the BPP model and explore customizable deployment areas and blockage penalties.

A. MCP model

To establish the simulation of the MCP model, we configure each cluster to have an average of 5 RIS panels. We assume each RIS panel has $M = 3000$ elements, and each RIS is serving 5 UEs. In other words, each UE is served by a batch of $M_o = 600$ RIS elements. The BS density is set as $10/\text{km}^2$ and we consider the typical UE to be served at a distance $r = 100\text{m}$. For the environment, we assume a Gaussian noise level of $\sigma_w^2 = 10^{-13}$ Watt.. The pathloss exponents are set to $\alpha_{\text{NLoS}} = 4$ for NLoS channels and $\alpha_{\text{LoS}} = 3$ for LoS channels in general, but the pathloss exponent for the reflected link across cells is specified as $\alpha_{I_R} = \{3, 3.5, 4\}$ for further investigation.

1) Impact of RIS reflection on interference: Deploying RIS clusters around all BSs can introduce inter-cell interference. Here, the intra-cell interference is neglected since we assume that the BSs can allocate the frequency resource to the UEs within their own cell. When RISs reflect the intended signals using narrow beams to the associated UEs, they might also reach the non-associated UEs in other cells that are reusing the same frequency band. The strength of inter-cell interference due to RIS reflection depends on the channel condition across cells

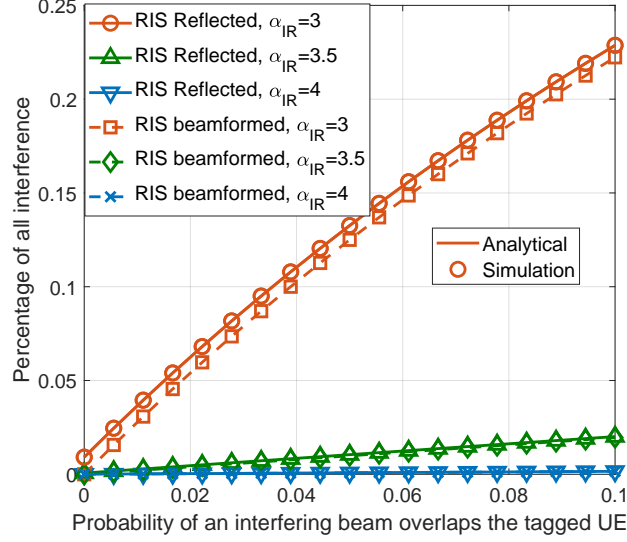


Fig. 6: Impact of overlapping probability and cross-cell channel condition on RIS reflected interference percentage

and the probability of the reflected beam reaching the typical UE, as discussed in Lemma 3. Such a dependency is quantitatively shown in Fig. 6, where the proportion of power of interference caused by RIS reflection is depicted⁸. When the inter-cell paths between RISs and the typical UE have nice channel conditions ($\alpha_{IR} = 3$), the reflected interference strength can be significant when a significant proportion of interfering beams are focused toward the typical UE. However, this case is rare in practice since the overlap probability should be low when the interfering beam is narrow and the beams are randomly directed in an arbitrary direction. In this analysis, we consider a conservative assumption where the beamwidth is 10 degrees out of 360 degrees, the overlapping probability is only 0.028. Thus, as shown in Fig. 6, the interference reflected from RISs is insignificant. Furthermore, in real-world scenarios, inter-cell channels are more likely to be worse than LoS links ($\alpha_{IR} = \{3.5, 4\}$). In these cases, the interference caused by RIS reflections is negligible compared to the interference from neighboring BSs, as suggested by the curves in Fig. 6. Based on the results, we can conclude that the interference reflected by RISs can be neglected when the reflected beam is narrow or the inter-cell channels are worse than LoS links ($\alpha_{IR} = 3.5 > \alpha_{LoS} = 3$).

2) *Network constraints: interference-limited or noise-limited:* To further analyze the overall impact of interference, we assess the ergodic rate of the typical UE based on either SIR or SINR metrics, considering whether reflected interference is included or not, and varying the transmitting power, as shown in Fig. 7. Specifically, to ensure a conservative estimate (where we intentionally overestimate the reflected interference), we focus on the scenario with the reflected beamwidth of 3.6° and the pathloss exponent for reflected paths $\alpha_{IR} = \{3, 3.5\}$, as detailed in the labels.

Figure 7 reveals two factors influencing whether a network is interference-limited: BS density and transmission power. We first take the SIR curve (with square-shaped markers) as the reference, since the transmitting power

⁸The value used to plot the relationship is computed by evaluating the first-order derivative of the Laplace transform at zero and further verified by Monte Carlo simulation.

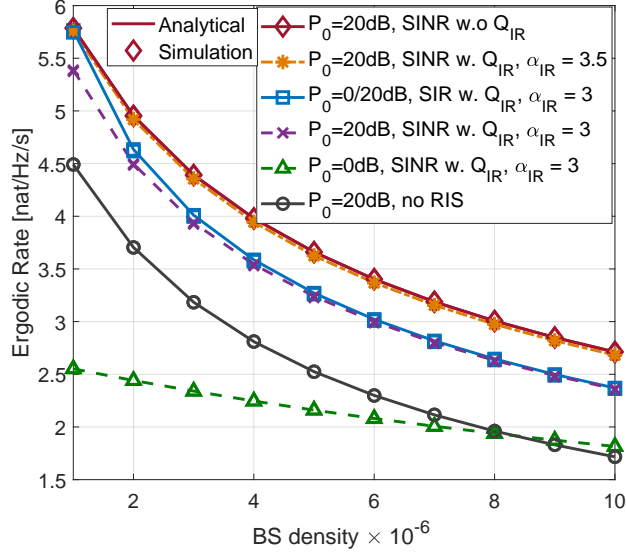


Fig. 7: Ergodic rate based on SNR, SIR, SINR, where interference can include the RIS reflected part or not

is then canceled in both the numerator and the denominator of the SIR fraction. We observe that the curves with transmitting power $P_0 = 20\text{dB}$ always show a similar trend as the SIR curve, implying that a high transmission power renders the network interference-limited as expected. However, the curve of $P_0 = 0\text{dB}$ has a different trend but converges to the SIR curve when the BS density is high. This is because, at low transmission power levels, cellular network performance is primarily limited by noise but when the BS density is high such as $10/\text{km}^2$, the interference level becomes comparable to the noise level and the network becomes interference-limited. Comparing the curve considering RIS reflected interference, i.e., w. Q_{I_R} (that with cross markers), against the curve w.o. Q_{I_R} (that with diamond markers), we observe that there is a gap between the curves, showing that when the pathloss of the reflected interference path is $\alpha_{I_R} = 3$, the reflected interference cannot be negligible. However, when we assume the reflected path is $\alpha_{I_R} = 3.5$, the curve with star markers almost overlaps with that with diamond markers showing that the RISs have a minimal effect on overall interference. This further validates the results in the previous simulation that the impact of inter-cell RIS reflected interference can be neglected when the pathloss of the reflected signal is large. These conditions are easily guaranteed since RIS is typically large, and a large number of elements will create a narrow beam, ensuring a low probability of overlap. Additionally, RIS deployment in practice is primarily directed at the associated UEs within their own cell, thus minimizing the possibility of generating interference that affects neighboring cells. To account for more realistic environment parameters, such as probabilistic blockage, we can use more complex channel models and incorporate them into our framework in future works.

3) *Network configuration*: In this paragraph, we evaluate the impact of the size of RIS w.r.t. the density of RISs when the total number of RIS elements per cluster is 10000. Since the RIS resources are shared, the size of RIS to perform the beamforming to the typical UE is inversely proportional to the density of the RISs. Fig. 8 plots the relationship between the ergodic rate and the density of RISs for serving the UE located at 100m from the

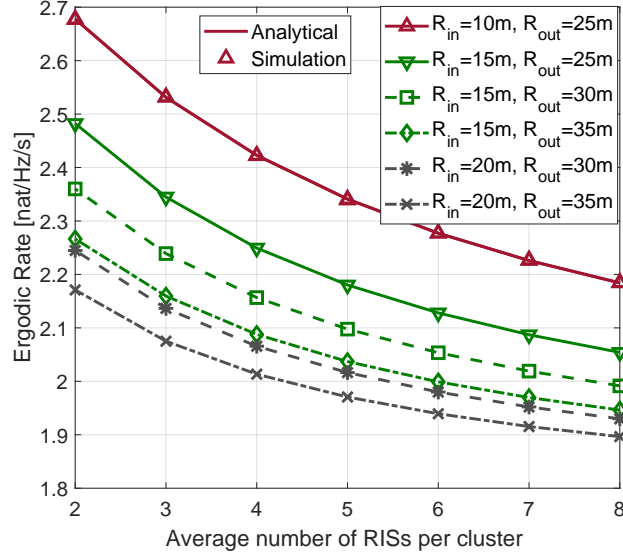


Fig. 8: Impact of the density of the RISs, when the total RIS resource is constant

associated BS. We observe the general trend that, in this setting, a higher RIS density leads to a lower ergodic rate, which shows that, at a system level, fewer but bigger RISs can assist the cellular system better than smaller but more numerous RISs. This is because the beamforming gain mainly depends on the number of the RIS elements of a batch available to form the beam. The results show that the spatial diversity gain is not as high as the beamforming gain. However, reflected beams might be blocked in a practical network. When considering potential blockage, a scenario with multiple, weaker reflected beams becomes more favorable for partial success than a single, powerful beam. Hence the diversity gain can outperform the beamforming gain.

Finally, we investigate the performance improvement w.r.t. different cluster radii. When the inner radius is set, the relative gains always decrease when the outer radius increases, implying that a smaller outer radius is favorable. On the other hand, comparing the line sets for the inner radius, the curves show that a smaller inner radius always outperforms a larger radius, suggesting the superiority of a smaller inner radius. Nevertheless, smaller cluster radii suggest that RISs should always be deployed close to the BS. This conclusion is valid for the current pathloss model without considering blockage. It is important to consider that, in real-world scenarios, obstacles blocking the direct link from the BS might also block the link associated with the RIS that is close to the BS. This shared blockage could limit the effectiveness of this particular RIS. Future research on blockage modeling should account for this possibility to refine the overall performance assessment.

B. Extensions and Variants

This subsection demonstrates the versatility of the framework introduced in Section IV. We evaluate the ergodic rate w.r.t. multiple variants: impact of blockage, wedge-shaped RIS deployment, and fixed RIS number. In the following, we focus on the impact of the spatial deployment of RISs in the associated cell and neglect the interference reflected from RISs in other cells, since we do not specify the deployment of RISs in their cell. This simplification

is reasonable in the case where the channel condition and the small beamwidth allow one to neglect the reflected interference from other cells, as shown in the conclusion about the reflected interference in the MCP model. We set the BS density to $\lambda_{\text{BS}} = 4/\text{km}^2$. The center of the coverage hole is located $r = 80\text{m}$ from the typical BS. This parameter ensures that the RISs are deployed within a distance less than half of the average distance between BSs. We set the inner radius to 25 meters and the outer radius to 35 meters, surrounding the coverage hole. RISs can be deployed over the whole ring, or refined in a wedge-shaped area of 90° , whose direction aligns with the center of the coverage hole. In addition to the PPP modeling, we also simulate the BPP to model the case of the fixed number of RISs with $N_{\text{RIS}} = 4$. Similar to the previous section, each RIS has $M = 3000$ elements to serve 5 UEs in this cell, i.e., each RIS serves each UE using $M_o = 600$ elements to form a narrow reflecting beam. Fig. 9 plots the relative gain when the direct link is affected by a constant blocking penalty C_D ranging from 0 to 5 dB and $C_R \in \{3, 5\}$ dB.

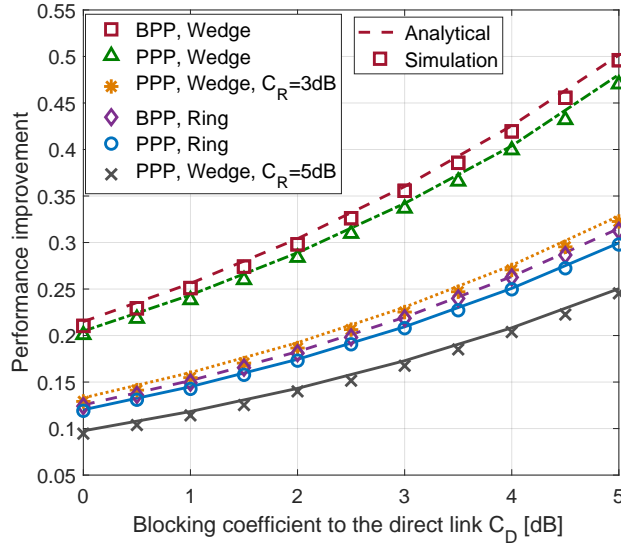


Fig. 9: Relative ergodic rate improvement in function of the blocking coefficient C_D .

In Fig. 9, the general trend shows that the improvement of the ergodic rate caused by the RISs will increase when the blocking coefficient attached to the direct link is larger, implying the importance of RISs for weak direct links. In other words, RISs can provide a significant gain in terms of ergodic rate when the direct link is severely blocked. Moreover, in the absence of blocking the reflected link, the use of a wedge-shaped area will increase the improvement resulting from RISs. This suggests that deploying RISs more strategically will introduce extra benefits. However, it is possible that the same obstacle can block both the direct link and the reflected links in this wedge-shaped layout. Introducing the blockage penalty $C_R = 3\text{dB}$ in the reflected links for the case of the wedge-shaped area can diminish the improvement. When $C_R = 5\text{dB}$, the improvement is even worse than deploying RISs over the ring. In addition, we observe that the improvement provided by a fixed number of RISs (modeled by BPP) is higher than that of a random number of RISs (modeled by PPP). This phenomenon shows that a fixed number of RISs should be preferred.

In practice, the deployment strategy depends on the scenarios and the corresponding statistics of the network. Real networks will impose constraints on the deployment area, penalties on the direct link, as well as the deployed number of RISs in a specific area. We can achieve system-level performance improvements by optimizing the set of parameters based on real-world information using the proposed framework.

VI. CONCLUSION

In this work, we provide a novel system-level analytical framework to evaluate the performance of a RIS-assisted network, where both BSs and RISs are modeled by spatial stochastic processes. This framework associates a set of RISs with a BS cell. It allows the parameters such as the deployment area, the number of RISs, and the size of RISs to be tuned based on deployment strategies. We focus on a BS-centric deployment modeled by MCP, for which we present the methodology for deriving the system metrics, i.e., the spectrum efficiency, based on the system parameters. Numerical results from the MCP model allow one to quantitatively investigate the role of the RIS reflections at a system level and understand the impact of the parameters for RIS deployment. We then extend the BS-centric MCP model to a UE-centric variant model, which accounts for the alleviation of coverage holes. Numerical results on this variant further provide insights into the design of RIS deployment in complex cellular networks. To sum up, the BS- and UE-centric models jointly demonstrate the capability and generality of the proposed framework in analyzing RIS-assisted networks. In future works, we will investigate the impact of randomly located blockages, the MIMO technique, and different propagation environments.

ACKNOWLEDGMENT

This work was supported by the CIFRE Ph.D. program, under the grant agreement 2021/0304 to NOKIA Network France. This work was also supported in part by the ERC NEMO grant, under the European Union's Horizon 2020 research and innovation programme, grant agreement number 788851 to INRIA, and by the French National Agency for Research (ANR) via the project ANR-22-PEFT-0010 of the French 2030 program PEPR - Réseaux du Futur.

APPENDIX

A. The small scale fading for the reflected link $\zeta = \rho_{R_1}\rho_{R_2}$

We discuss the random variable $\zeta \in \mathbb{C}$ that represents the composite small-scale fading of the signal that is reflected by a RIS element [49]. Since we assume that the fading of the link from the BS to the RIS is independent of that of the link from the RIS to the UE, ζ is the product of two independent small-scale fading variables ρ_R , given by

$$\zeta = \rho_{R_1}\rho_{R_2} = |\rho_{R_1}| \cdot |\rho_{R_2}| \cdot e^{i(\theta_{R_1} + \theta_{R_2})} \in \mathbb{C}. \quad (40)$$

According to the fading assumption, the signal reflected by one RIS element experiences two consecutive Rician fades, in the case where the links from the BS to the RISs and from the RISs to the UE have LoS channel conditions. Nevertheless, the reflected signal, either arriving at the receiver antenna in-phase when beamformed or out-of-phase when scattered from an RIS, is the superposition of reflection from a large number of elements of that same RIS. Since the path loss of the reflected path via the same RIS is of the same order, we will later apply the

central limit theorem for the superposed fading so that the first two moments of the $|\zeta|$ are sufficient to characterize the superposed reflected signal. Classical results [50] on the mean and variance of the product of independently distributed random variables,

$$\mathbb{E}[|\rho_{R_1}| \cdot |\rho_{R_2}|] = \mathbb{E}[X_1]\mathbb{E}[X_2],$$

$$\mathbb{V}[|\rho_{R_1}| \cdot |\rho_{R_2}|] = \mathbb{V}[X_1]\mathbb{V}[X_2] + \mathbb{V}[X_1]\mathbb{E}[X_2]^2 + \mathbb{V}[X_2]\mathbb{E}[X_1]^2.$$

For example, we assume the Rician factor⁹ of the Rician fading is one in the simulation, without loss of generality, and that the magnitude of fading for each link is distributed as $|\rho| \sim \left| \sqrt{\frac{1}{2}} + \sqrt{\frac{1}{2}}\mathcal{CN}(0,1) \right|$. We have $\mathbb{E}[|\rho_R|] = \sqrt{\frac{\pi}{8}} {}_1F_1(-\frac{1}{2}; 1; -1)$ and $\mathbb{V}[|\rho_R|] = 1 - \frac{\pi}{8} {}_1F_1(-\frac{1}{2}; 1; -1)^2$. Using the above results, we get

$$\mathbb{E}[|\zeta|] = \frac{\pi}{8} \left({}_1F_1\left(-\frac{1}{2}, 1, -1\right) \right)^2, \quad \mathbb{V}[|\zeta|] = 1 - \left(\frac{\pi}{8} \left({}_1F_1\left(-\frac{1}{2}, 1, -1\right) \right)^2 \right)^2, \quad (41)$$

where ${}_1F_1(\cdot, \cdot, \cdot)$ denotes the confluent hypergeometric function [51].

B. Laplace transform of the aggregated interference $\mathcal{L}_{TQ_i(r)}(s)$

The typical UE receives interference from the BSs and the RISs in other cells. We characterize the interference in terms of Laplace transform in two steps. We begin by analyzing a single cell, calculating the distribution of the interference power from the BS and the randomly located RISs in that cell. Then, we express the total interference combined from all cells.

The interference power from the i^{th} cell is given by $Q_{c_i} = \gamma_{I_{D_i}} P_0 g(\|\mathbf{x}_i\|) + \sum_{j \in \mathcal{J}_i} \gamma_{I_{R_{i,j}}} P_0 G(\mathbf{x}_i, \mathbf{y}_{i,j})$. Let $x_i = \|\mathbf{x}_i\|$ denote the distance between the BS of that cell to the typical UE, we have the Laplace transform of the scaled interference TQ_{c_i} of this cell

$$\begin{aligned} \mathcal{L}_{TQ_{c_i}}(s) &= \mathbb{E}_{\gamma_{I_{D_i}}, \gamma_{I_{R_{i,j}}}, \phi_i} \left[\exp \left(-sT\gamma_{I_{D_i}} P_0 g(x_i) - \sum_{j \in \mathcal{J}_i} sT\gamma_{I_{R_{i,j}}} P_0 G(\mathbf{x}_i, \mathbf{y}_{i,j}) \right) \right] \\ &= \mathbb{E}_{\gamma_{I_{D_i}}} \left[\exp \left(-s\gamma_{I_{D_i}} P_0 Tg(x_i) \right) \right] \cdot \mathbb{E}_{\gamma_{I_{R_{i,j}}}, \phi_i} \left[\exp \left(- \sum_{j \in \mathcal{J}_i} s\gamma_{I_{R_{i,j}}} P_0 TG(\mathbf{x}_i, \mathbf{y}_{i,j}) \right) \right] \\ &\stackrel{(a)}{=} \mathcal{L}_{\gamma_{I_{D_i}}}(sP_0 Tg(x_i)) \cdot \mathbb{E}_{\gamma_{I_{R_{i,j}}}, \phi_i} \left[\exp \left(- \sum_{j \in \mathcal{J}_i} s\gamma_{I_{R_{i,j}}} P_0 TG(\mathbf{x}_i, \mathbf{y}_{i,j}) \right) \middle| O_{\text{beam}} \right]. \\ &\quad \mathbb{E}_{\gamma_{I_{R_{i,j}}}, \phi_i} \left[\exp \left(- \sum_{j \in \mathcal{J}_i} s\gamma_{I_{R_{i,j}}} P_0 TG(\mathbf{x}_i, \mathbf{y}_{i,j}) \right) \middle| \bar{O}_{\text{beam}} \right] \\ &\stackrel{(b)}{=} \frac{1}{1 + sP_0 Tg(x_i)} \exp \left(\frac{\vartheta_{\text{beam}}}{2\pi} \lambda_{\text{RIS}} \int_0^{2\pi} \int_{R_{\text{in}}}^{R_{\text{out}}} \left(1 - \mathcal{L}_{\gamma_{S_R}}(sP_0 TG(x_i, y, \psi)) \right) dy d\theta \right) \\ &\quad \exp \left(\left(1 - \frac{\vartheta_{\text{beam}}}{2\pi} \right) \lambda_{\text{RIS}} \int_0^{2\pi} \int_{R_{\text{in}}}^{R_{\text{out}}} \left(1 - \frac{1}{1 + s(M - M_o)P_0 TG(x_i, y, \psi)} \right) dy d\theta \right). \end{aligned} \quad (42)$$

where $\mathcal{L}_{\gamma_{S_R}}(s)$ is given in Lemma 2. Here in (a), we use the fact that the reflected interference from any given RIS arrives at the typical UE in either the beamformed part or the scattered part. If the typical UE is within the interference beam, we denote the event as O_{beam} . Otherwise, the event of experiencing the scattered interference is denoted as \bar{O}_{beam} . They are modeled by two thinning Poisson point processes with the density $\frac{\vartheta_{\text{beam}}}{2\pi} \lambda_{\text{RIS}}$ and

⁹The ratio of the energy of the LoS component to that of the scattered component [16].

$(1 - \frac{\vartheta_{\text{beam}}}{2\pi})\lambda_{\text{RIS}}$, respectively, where $\frac{\vartheta_{\text{beam}}}{2\pi}$ is the fraction of beam over the total angular domain 2π . (b) follows from the fact that ϕ_i are Poisson point process and $\gamma_{I_{R_i}}$ are i.i.d. fading, thus we can apply the PGFL of the PPP that $\mathbb{E}[\prod_{x \in \Phi} f(x)] \stackrel{\Phi: \text{PPP}}{=} \exp(-\lambda \int_{\mathbb{R}^2} (1 - f(x)) dx)$, where \mathbb{R}^2 denotes the Euclidean space in which the PPP is distributed.

Next, we compute the Laplace transform of the total interference based on $Q_I(r) = \sum_{i \in \mathcal{I} \setminus o} Q_{c_i}$, given by

$$\begin{aligned} \mathcal{L}_{TQ_I(r)}(s) &= \mathbb{E} \left[e^{-sTQ_I(r)} \middle| r \right] \\ &= \mathbb{E}_{\Phi_{\text{BS}} \setminus \mathbf{x}_o, \gamma_{I_i}} \left[\exp \left(-sT \sum_{i \neq o} Q_{c_i} \right) \right] \stackrel{(a)}{=} \mathbb{E}_{\Phi_{\text{BS}}} \left[\prod_{i \neq o} \mathbb{E}_{Q_{c_i}} \left[\exp \left(-sTQ_{c_i} \right) \right] \right] \\ &\stackrel{(b)}{=} \exp \left(-2\pi\lambda_{\text{BS}} \int_r^\infty x \left(1 - \mathbb{E}_{Q_{c_i}} \left[\exp \left(-sTQ_{c_i} \right) \right] \right) dx \right) \\ &\stackrel{(c)}{=} \exp \left(-2\pi\lambda_{\text{BS}} \int_r^\infty x \left(1 - \mathcal{L}_{TQ_{c_i}(x)}(s) \right) dx \right), \end{aligned} \quad (43)$$

where (a) follows from the i.i.d. distribution of the fadings Q_{c_i} and its independence from the mother point process Φ_{BS} defining the random placement of the BSs; (b) follows from the probability generating functional (PGFL) of the PPP. Here, the isotropy of PPP allows the polar coordinates in (b), and the integration limits are from r to ∞ since the closest cluster head is at a distance r . Plugging the Laplace transform of a cell in Eq. (42) gives (c). Note that Q_{c_i} is the function of the distance x_i to the BS of that cell, the functional of the Laplace transform is $Q_c(x)$.

C. Region of convergence for the Laplace transform $\mathcal{B}_\Upsilon(s)$

The prerequisite to applying the proposed analytical method is to guarantee that the bilateral Laplace transform $\mathcal{B}_\Upsilon(s)$ exists, namely the argument of the Laplace functional is defined in the domain where Laplace transform is convergent. By definition, the region of convergence of a bilateral Laplace transforms $\mathcal{B}_\Upsilon(s) = \int_{-\infty}^\infty f(t)e^{-st} dt$ is a vertical strip in the complex s -plane [48, Chapter VI], i.e., $s_a < \Re(s) < s_b$ with $s_a < s_b$. In addition, $\mathcal{B}_\Upsilon(s)$ is given by $\mathcal{B}_\Upsilon(s) = \mathcal{B}_{TQ_I(r)}(s)\mathcal{B}_{T\sigma_w^2}(s)\mathcal{B}_{-Q_{S_R}(r)}(s)$, due to the composition rule of $\Upsilon = TQ_I(r) + T\sigma_w^2 - Q_{S_R}(r)$. The facts that the interference $TQ_I(r) + T\sigma_w^2$ is non-negative and $-Q_{S_R}(r)$ is non-positive give that $\mathcal{B}_{TQ_I(r)}(s)\mathcal{B}_{T\sigma_w^2}(s) = \mathcal{L}_{TQ_I(r)}(s)\mathcal{L}_{T\sigma_w^2}(s)$ and $\mathcal{B}_{-Q_{S_R}(r)}(s) = \mathcal{L}_{-Q_{S_R}(r)}(s)$, respectively. Therefore, the region of convergence of s is the intersection of the right half plane $\Re(s) > s_a$ as the region of convergence for $\mathcal{L}_{TQ_I(r)}(s)\mathcal{L}_{T\sigma_w^2}(s)$ and the left half plane $\Re(s) < s_b$ for $\mathcal{L}_{-Q_{S_R}(r)}(s)$.

Due to the characteristic function of any PDF exists, we have $s_a < 0 < s_b$. In addition, the argument-to-evaluate of the Laplace transform for computing the coverage probability is $s = \frac{1}{P_0 g(r)} > 0$, as given in Eq. (34). Therefore, we focus on discussing s_b imposed by the reflected signal field since the region of interest is $0 < \Re(s) < s_b$. In other words, the value of s_a does not impact the convergence behavior. To identify the constraint of s_b , we investigate the condition that ensures the convergence of the Laplace transform $\mathcal{L}_{-Q_{S_R}(r)}(s)$, given in Eq. (31)

$$\begin{aligned} \mathcal{L}_{-Q_{S_R}(r)}(s) &= e^{-\lambda_{\text{RIS}} \int_0^{2\pi} \int_{R_{\text{in}}}^{R_{\text{out}}} y \left(1 - \mathcal{L}_{\gamma_{S_R}} \left[-sP_0 \mathcal{G}(x, y, \psi) \right] \right) dy d\theta} \\ &\stackrel{(a)}{=} e^{-\lambda_{\text{RIS}} \int_0^{2\pi} \int_{R_{\text{in}}}^{R_{\text{out}}} y \left(1 - \mathcal{L}_{\gamma_{S_R}} \left[-\frac{\mathcal{G}(x, y, \psi)}{g(r)} \right] \right) dy d\theta}, \end{aligned} \quad (44)$$

where r is the distance from the nearest BS to the typical UE, and (a) follows from that $s = \frac{1}{P_0 g(r)}$.

The condition that the Laplace transform of the distribution function of the reflecting fading is convergent specifies that $-\frac{\mathcal{G}(r,y,\psi)}{g(r)}$ is in the region of convergence for γ_{SR} . According to the fact that the region of convergence for the Laplace transform of the PDF of a standard non-central χ^2 distribution is $s > -\frac{1}{2}$ and that of an exponential distribution is $s > -1$. Inserting variance σ_{\Re}^2 defined in Lemma 2, we have the implicit constraints that

$$\frac{(M + M_o)\mathbb{V}[\zeta]\mathcal{G}(r, y, \psi)}{2g(r)} < \frac{1}{2}. \quad (45)$$

When the parameters of the network satisfy the constraints in Eq. (45), we could apply the analytical method to assess the network performance. The analytical constraints establish the feasible region for applying this methodology. All subsequent analyses must ensure parameters remain within this defined region.

D. Expressing $\mathcal{L}_{\Upsilon^+}(s)$ in function of $\mathcal{B}_{\Upsilon}(s)$

For a real-valued variable $x \in \mathbb{R}$ and $x^+ = \max\{x, 0\}$, the following identity holds based on some manipulations of the sign function and e^{-sx} [52],

$$e^{-sx^+} - e^{-sx} = \frac{1}{2}(e^{-s \cdot 0} - e^{-sx})(1 - \text{sign}(x)), \quad (46)$$

where the sign function is defined by

$$\text{sign}(x) = \begin{cases} 0, & x < 0, \\ 1, & x \geq 0. \end{cases}$$

Using the identity $\int_{-\infty}^{\infty} \frac{\sin(ux)}{u} du = \pi \text{sign}(x)$ and $x^+ = \frac{x}{2}(1 + \text{sign}(x))$, it follows that

$$\begin{aligned} e^{-sx^+} &= \frac{1}{2} \left(1 + e^{-sx} - (1 - e^{-sx}) \cdot \text{sign}(x) \right) \\ &= \frac{1}{2} \left(1 + e^{-sx} - (1 - e^{-sx}) \frac{1}{\pi} \int_{-\infty}^{\infty} \frac{\sin(ux)}{u} du \right) \\ &\stackrel{(a)}{=} \frac{1}{2} \left(1 + e^{-sx} - (1 - e^{-sx}) \frac{1}{\pi} \int_{-\infty}^{\infty} \frac{e^{\imath ux} - e^{-\imath ux}}{2\imath u} du \right) \\ &= \frac{1}{2} \left(1 + e^{-sx} + \frac{1}{2\pi\imath} \int_{-\infty}^{\infty} \left(e^{-sx+\imath ux} - e^{-sx-\imath ux} - e^{\imath ux} + e^{-\imath ux} \right) \frac{du}{u} \right) \\ &\stackrel{(b)}{=} \frac{1}{2} \left(1 + e^{-sx} + \frac{1}{\pi\imath} \int_{-\infty}^{\infty} \left(e^{-sx+\imath ux} - e^{\imath ux} \right) \frac{du}{u} \right), \end{aligned} \quad (47)$$

where (a) follows from the Euler formula $\sin(x) = \frac{e^{\imath x} - e^{-\imath x}}{2\imath}$, and (b) follows from the fact that the integral defined in the principal value sense is an odd symmetric function.

Applying the expectation operator $\mathbb{E}[\cdot]$ over both side of Eq. (47), we have

$$\begin{aligned} \mathcal{B}_{\Upsilon^+}(s) &= \mathbb{E} \left[e^{-s\Upsilon^+} \right] = \int_{-\infty}^{\infty} e^{-sx^+} f_{\Upsilon}(x) dx \\ &= \int_{-\infty}^{\infty} \left[\frac{1}{2} \left(1 + e^{-sx} + \frac{1}{\pi\imath} \int_{-\infty}^{\infty} \left(e^{-sx+\imath ux} - e^{\imath ux} \right) \frac{du}{u} \right) \right] f_{\Upsilon}(x) dx \\ &\stackrel{(a)}{=} \frac{1}{2} \left(1 + \int_{-\infty}^{\infty} e^{-sx} f_{\Upsilon}(x) dx + \frac{1}{\pi\imath} \int_{-\infty}^{\infty} \left(\int_{-\infty}^{\infty} e^{-sx+\imath ux} f_{\Upsilon}(x) dx - \int_{-\infty}^{\infty} e^{\imath ux} f_{\Upsilon}(x) dx \right) \frac{du}{u} \right) \\ &= \frac{1}{2} \left(1 + \mathcal{B}_{\Upsilon}(s) + \frac{1}{\pi\imath} \int_{-\infty}^{\infty} \left(\mathcal{B}_{\Upsilon}(s - \imath u) - \mathcal{B}_{\Upsilon}(-\imath u) \right) \frac{du}{u} \right), \end{aligned} \quad (48)$$

when s is in the region of convergence, which is discussed in Appendix. C.

Next, by the definition of the unilateral and bilateral Laplace transform of the PDF $f_{\Upsilon}(x)$, we can express

$$\begin{aligned}\mathcal{L}_{\Upsilon^+}(s) &= \int_0^{\infty} e^{-sx^+} f_{\Upsilon}(x) dx = \int_{-\infty}^{\infty} e^{-sx^+} f_{\Upsilon}(x) dx - \int_{-\infty}^0 f_{\Upsilon}(x) dx \\ &= \mathcal{B}_{\Upsilon^+}(s) - \mathbb{P}[\Upsilon < 0] \stackrel{(a)}{=} \mathcal{B}_{\Upsilon^+}(s) - \mathcal{B}_{\mathcal{B}_{\Upsilon}(s)/s}^{-1}(0),\end{aligned}\tag{49}$$

where (a) follows from the CDF is the inverse Laplace transform of $\frac{1}{s}\mathcal{B}_{f(x)}(s)$ due to the property of time-domain integration of Laplace transform $\mathcal{B}_{\int_{-\infty}^{\infty} f(x) dx}(s) = \frac{1}{s}\mathcal{B}_{f(x)}(s)$, with the support of s is $\text{Re}(s) > 0$.

Combining Eq. (48) and Eq. (49), Eq. (32) is proved.

REFERENCES

- [1] K. David and H. Berndt, "6G vision and requirements: Is there any need for beyond 5G?," *IEEE vehicular technology magazine*, vol. 13, no. 3, pp. 72–80, 2018.
- [2] A. Shaikh and M. J. Kaur, "Comprehensive survey of massive MIMO for 5G communications," in *2019 Advances in Science and Engineering Technology International Conferences (ASET)*, pp. 1–5, IEEE, 2019.
- [3] B. T. Jijo, S. R. Zeebaree, R. R. Zebari, M. A. Sadeeq, A. B. Sallow, S. Mohsin, and Z. S. Ageed, "A comprehensive survey of 5G mm-wave technology design challenges," *Asian Journal of Research in Computer Science*, vol. 8, no. 1, pp. 1–20, 2021.
- [4] F. Grijpink, A. Ménard, H. Sigurdsson, and N. Vucevic, "The road to 5G: The inevitable growth of infrastructure cost," 2018.
- [5] I. P. Chochliouros, M.-A. Kourtis, A. S. Spiliopoulou, P. Lazaridis, Z. Zaharis, C. Zarakovitis, and A. Kourtis, "Energy efficiency concerns and trends in future 5G network infrastructures," *Energies*, vol. 14, no. 17, p. 5392, 2021.
- [6] D. Xu, A. Zhou, X. Zhang, G. Wang, X. Liu, C. An, Y. Shi, L. Liu, and H. Ma, "Understanding operational 5g: A first measurement study on its coverage, performance and energy consumption," in *Proceedings of the Annual conference of the ACM Special Interest Group on Data Communication on the applications, technologies, architectures, and protocols for computer communication*, pp. 479–494, 2020.
- [7] T. Sharma, A. Chehri, and P. Fortier, "Reconfigurable intelligent surfaces for 5g and beyond wireless communications: A comprehensive survey," *Energies*, vol. 14, no. 24, p. 8219, 2021.
- [8] G. C. Alexandropoulos, G. Lerosey, M. Debbah, and M. Fink, "Reconfigurable intelligent surfaces and metamaterials: The potential of wave propagation control for 6G wireless communications," *arXiv preprint arXiv:2006.11136*, 2020.
- [9] L. Dai, B. Wang, M. Wang, X. Yang, J. Tan, S. Bi, S. Xu, F. Yang, Z. Chen, M. Di Renzo, *et al.*, "Reconfigurable intelligent surface-based wireless communications: Antenna design, prototyping, and experimental results," *IEEE access*, vol. 8, pp. 45913–45923, 2020.
- [10] M. D. Renzo, M. Debbah, D.-T. Phan-Huy, A. Zappone, M.-S. Alouini, C. Yuen, V. Sciancalepore, G. C. Alexandropoulos, J. Hoydis, H. Gacanin, *et al.*, "Smart radio environments empowered by reconfigurable ai meta-surfaces: An idea whose time has come," *EURASIP Journal on Wireless Communications and Networking*, vol. 2019, no. 1, pp. 1–20, 2019.
- [11] M. Di Renzo, K. Ntontin, J. Song, F. H. Danufane, X. Qian, F. Lazarakis, J. De Rosny, D.-T. Phan-Huy, O. Simeone, R. Zhang, *et al.*, "Reconfigurable intelligent surfaces vs. relaying: Differences, similarities, and performance comparison," *IEEE Open Journal of the Communications Society*, vol. 1, pp. 798–807, 2020.
- [12] J. Ye, A. Kammoun, and M.-S. Alouini, "Spatially-distributed RISs vs relay-assisted systems: A fair comparison," *IEEE Open Journal of the Communications Society*, vol. 2, pp. 799–817, 2021.
- [13] S. Lin, B. Zheng, G. C. Alexandropoulos, M. Wen, F. Chen, *et al.*, "Adaptive transmission for reconfigurable intelligent surface-assisted OFDM wireless communications," *IEEE Journal on Selected Areas in Communications*, vol. 38, no. 11, pp. 2653–2665, 2020.
- [14] H. Lu, Y. Zeng, S. Jin, and R. Zhang, "Single-carrier delay alignment modulation for multi-irs aided communication," *IEEE Transactions on Wireless Communications*, 2023.
- [15] B. Furht and S. A. Ahson, *Long Term Evolution: 3GPP LTE radio and cellular technology*. Crc Press, 2016.
- [16] D. Tse and P. Viswanath, *Fundamentals of wireless communication*. Cambridge university press, 2005.
- [17] E. Shtaiwi, H. Zhang, S. Vishwanath, M. Youssef, A. Abdelhadi, and Z. Han, "Channel estimation approach for RIS assisted MIMO systems," *IEEE Transactions on Cognitive Communications and Networking*, vol. 7, no. 2, pp. 452–465, 2021.
- [18] Ö. Özdogan, E. Björnson, and E. G. Larsson, "Intelligent reflecting surfaces: Physics, propagation, and pathloss modeling," *IEEE Wireless Communications Letters*, vol. 9, no. 5, pp. 581–585, 2019.

- [19] J. Chen, Y.-C. Liang, H. V. Cheng, and W. Yu, "Channel estimation for reconfigurable intelligent surface aided multi-user MIMO systems," *arXiv preprint arXiv:1912.03619*, 2019.
- [20] C. Huang, A. Zappone, G. C. Alexandropoulos, M. Debbah, and C. Yuen, "Reconfigurable intelligent surfaces for energy efficiency in wireless communication," *IEEE Transactions on Wireless Communications*, vol. 18, no. 8, pp. 4157–4170, 2019.
- [21] Q. Wu and R. Zhang, "Intelligent reflecting surface enhanced wireless network via joint active and passive beamforming," *IEEE Transactions on Wireless Communications*, vol. 18, no. 11, pp. 5394–5409, 2019.
- [22] S. Zeng, H. Zhang, B. Di, Z. Han, and L. Song, "Reconfigurable intelligent surface (RIS) assisted wireless coverage extension: RIS orientation and location optimization," *IEEE Communications Letters*, vol. 25, no. 1, pp. 269–273, 2020.
- [23] S. Abeywickrama, R. Zhang, Q. Wu, and C. Yuen, "Intelligent reflecting surface: Practical phase shift model and beamforming optimization," *IEEE Transactions on Communications*, vol. 68, no. 9, pp. 5849–5863, 2020.
- [24] X. Tan, Z. Sun, J. M. Jornet, and D. Pados, "Increasing indoor spectrum sharing capacity using smart reflect-array," in *2016 IEEE International Conference on Communications (ICC)*, pp. 1–6, IEEE, 2016.
- [25] A. Kammoun, A. Chaaban, M. Debbah, M.-S. Alouini, *et al.*, "Asymptotic max-min SINR analysis of reconfigurable intelligent surface assisted MISO systems," *IEEE Transactions on Wireless Communications*, vol. 19, no. 12, pp. 7748–7764, 2020.
- [26] H. Wang, S. Ma, T.-S. Ng, and H. V. Poor, "A general analytical approach for opportunistic cooperative systems with spatially random relays," *IEEE Transactions on Wireless Communications*, vol. 10, no. 12, pp. 4122–4129, 2011.
- [27] Z. Ding, I. Krikidis, B. Sharif, and H. V. Poor, "Wireless information and power transfer in cooperative networks with spatially random relays," *IEEE Transactions on Wireless Communications*, vol. 13, no. 8, pp. 4440–4453, 2014.
- [28] M. A. Kishk and M.-S. Alouini, "Exploiting randomly located blockages for large-scale deployment of intelligent surfaces," *IEEE Journal on Selected Areas in Communications*, vol. 39, no. 4, pp. 1043–1056, 2020.
- [29] Y. Zhu, G. Zheng, and K.-K. Wong, "Stochastic geometry analysis of large intelligent surface-assisted millimeter wave networks," *IEEE Journal on Selected Areas in Communications*, vol. 38, no. 8, pp. 1749–1762, 2020.
- [30] M. Di Renzo and J. Song, "Reflection probability in wireless networks with metasurface-coated environmental objects: An approach based on random spatial processes," *EURASIP Journal on Wireless Communications and Networking*, vol. 2019, no. 1, pp. 1–15, 2019.
- [31] G. Ghatak, V. Malik, S. S. Kalamkar, and A. K. Gupta, "Where to deploy reconfigurable intelligent surfaces in the presence of blockages?," in *2021 IEEE 32nd Annual International Symposium on Personal, Indoor and Mobile Radio Communications (PIMRC)*, pp. 1419–1424, IEEE, 2021.
- [32] J. Lyu and R. Zhang, "Hybrid active/passive wireless network aided by intelligent reflecting surface: System modeling and performance analysis," *IEEE Transactions on Wireless Communications*, vol. 20, no. 11, pp. 7196–7212, 2021.
- [33] C. Zhang, W. Yi, Y. Liu, K. Yang, and Z. Ding, "Reconfigurable intelligent surfaces aided multi-cell noma networks: A stochastic geometry model," *IEEE Transactions on Communications*, vol. 70, no. 2, pp. 951–966, 2021.
- [34] T. Wang, G. Chen, M.-A. Badiu, and J. P. Coon, "Performance analysis of RIS-assisted large-scale wireless networks using stochastic geometry," *IEEE Transactions on Wireless Communications*, 2023.
- [35] N. Deng, J. Qi, H. Wei, N. Zhao, and D. Niyato, "Modeling and Analysis of IRS-Assisted networks based on gauss-poisson process," *IEEE Transactions on Wireless Communications*, 2024.
- [36] J. G. Andrews, F. Baccelli, and R. K. Ganti, "A tractable approach to coverage and rate in cellular networks," *IEEE Transactions on communications*, vol. 59, no. 11, pp. 3122–3134, 2011.
- [37] F. Baccelli, B. Błaszczyszyn, *et al.*, "Stochastic geometry and wireless networks: Volume II applications," *Foundations and Trends® in Networking*, vol. 4, no. 1–2, pp. 1–312, 2010.
- [38] F. Baccelli, B. Błaszczyszyn, and M. Karray, "Random measures, point processes, and stochastic geometry," 2020.
- [39] J. G. Andrews, A. K. Gupta, and H. S. Dhillon, "A primer on cellular network analysis using stochastic geometry," *arXiv preprint arXiv:1604.03183*, 2016.
- [40] I. S. G. ISG, "Reconfigurable Intelligent Surfaces (RIS): Communication Models, Channel Models, Channel Estimation and Evaluation Methodology," Jun 2023.
- [41] S. Zeng, H. Zhang, B. Di, Y. Tan, Z. Han, H. V. Poor, and L. Song, "Reconfigurable intelligent surfaces in 6G: Reflective, transmissive, or both?," *IEEE Communications Letters*, vol. 25, no. 6, pp. 2063–2067, 2021.
- [42] J. An, C. Xu, D. W. K. Ng, C. Yuen, L. Gan, and L. Hanzo, "Reconfigurable intelligent surface-enhanced OFDM communications via delay adjustable metasurface," *arXiv preprint arXiv:2110.09291*, 2021.

- [43] G. Wu, F. Li, and H. Jiang, "Analysis of multipath fading and doppler effect with multiple reconfigurable intelligent surfaces in mobile wireless networks," *Wireless Communications and Mobile Computing*, vol. 2022, pp. 1–15, 2022.
- [44] E. Björnson and L. Sanguinetti, "Rayleigh fading modeling and channel hardening for reconfigurable intelligent surfaces," *IEEE Wireless Communications Letters*, vol. 10, no. 4, pp. 830–834, 2020.
- [45] M. K. Simon, *Probability distributions involving Gaussian random variables: A handbook for engineers and scientists*. Springer, 2002.
- [46] H. Han, Y. Liu, and L. Zhang, "On half-power beamwidth of intelligent reflecting surface," *IEEE Communications Letters*, vol. 25, no. 4, pp. 1333–1337, 2020.
- [47] A. V. Oppenheim, J. Buck, M. Daniel, A. S. Willsky, S. H. Nawab, and A. Singer, *Signals & systems*. Pearson Educación, 1997.
- [48] D. V. Widder, *Laplace transform (PMS-6)*, vol. 64. Princeton university press, 2015.
- [49] X. Qian, M. Di Renzo, J. Liu, A. Kammoun, and M.-S. Alouini, "Beamforming through reconfigurable intelligent surfaces in single-user MIMO systems: SNR distribution and scaling laws in the presence of channel fading and phase noise," *IEEE wireless communications letters*, vol. 10, no. 1, pp. 77–81, 2020.
- [50] M. D. Springer, "The algebra of random variables," (*No Title*), 1979.
- [51] G. E. Andrews, R. Askey, and R. Roy, *Special Functions*. No. 71, Cambridge University Press, 1999.
- [52] I. Pinelis, "Characteristic function of the positive part of a random variable and related results, with applications," *Statistics & Probability Letters*, vol. 106, pp. 281–286, 2015.